Engineering Linear Cap-independent mRNA Vaccines with Intrinsic Adjuvanticity for Potent Cancer Immunotherapy

Hongwu Yu[1,2]*, Yu Yang[1,2]*, Peng Lin[1,2], Chengye Liu[1,2], Yifan Wen[1,2], Zhuting Fang[3]✉, Zhixiang Hu[1,2]✉, Shenglin Huang[1,2,4]✉

[1]Department of Integrative Oncology, Fudan University Shanghai Cancer Center, and Shanghai Key Laboratory of Medical Epigenetics, Institutes of Biomedical Sciences, Fudan University, Shanghai, 200032, China.

[2]Department of Oncology, Shanghai Medical College, Fudan University, Shanghai, 200032, China.

[3]Department of Oncology and Vascular Interventional Therapy, Clinical Oncology School of Fujian Medical University, Fujian Cancer Hospital (Fujian Branch of Fudan University Shanghai Cancer Center), Fuzhou, 350014, China.

[4]State Key Laboratory of Genetics and Development of Complex Phenotypes, Fudan University, Shanghai, China.

*These authors contributed equally to the manuscript.

✉Corresponding authors: Zhuting Fang, Ph.D, Prof. E-mail: ztfang@fjzlhospital.com; Zhixiang Hu, Ph.D, Prof. Email: zhixiang_hu@fudan.edu.cn; Shenglin Huang, Ph.D, Prof. E-mail: slhuang@fudan.edu.cn.

ABSTRACT

mRNA cancer vaccines have shown promising efficacy in early-phase clinical trials, but existing platforms struggle to boost antitumor efficacy without added cost or complexity. Here, we present a streamlined linear cap-independent RNA (LciRNA) cancer vaccine platform that achieves stable expression *in vivo* without 5' capping or ribonucleotide modification, and innately stimulates immune responses to enhance antitumor immunity. By fusing a UPA protective sequence, composed of a viral exoribonuclease-resistant RNA (xrRNA) and a poly(A) binding protein (PABP) motif, with an optimized *Enterovirus* A internal ribosome entry site, LciRNA resists 5' exonuclease decay and drives superior *in vivo* expression. Mechanistically, UPA sequence not only impedes exonuclease-mediated decay but also recruits RNA-binding proteins to stabilize LciRNA. Moreover, LciRNA robustly activates dendritic cell pattern-recognition receptor pathways, promotes dendritic cell maturation, and upregulates proinflammatory signals. In murine melanoma and HPV-associated tumor models, it elicits strong systemic and intra-tumoral T cell responses and superior tumor control, demonstrating how immune stimulation-translation synergy underpins its efficacy. This work establishes a next-generation cost-effective mRNA cancer vaccine platform with simplified production and enhanced efficacy, highlighting immuno-translation coupling as a paradigm for future mRNA cancer vaccines.

Keywords:

mRNA; Cancer immunotherapy; Cancer vaccines; Cap-independent translation; Subgenomic flaviviral RNA

46 **INTRODUCTION**

47

48 Messenger RNA (mRNA) has emerged as a transformative vaccine platform owing to its rapid
49 development, robust immunogenicity, and favorable safety profile. The successful application of
50 mRNA vaccines during the COVID-19 pandemic demonstrated their exceptional safety and superior
51 protective efficacy compared with traditional modalities[1]. Accordingly, mRNA technology is being
52 actively explored for oncological applications, where it is anticipated to enable the development of
53 a new generation of transformative cancer therapeutics[2,3]. Recent clinical results underscore this
54 promise. In a Phase IIb trial, the personalized vaccine mRNA-4157 plus pembrolizumab reduced
55 the risk of recurrence or death by 44% in advanced melanoma patients[4]. Similarly, the personalized
56 vaccine BNT-122 induced markedly prolonged median recurrence-free survival (RFS) in responders
57 in a Phase I adjuvant trial for pancreatic ductal adenocarcinoma, and elicited long-lived effector T
58 cell clones with an estimated lifespan of 7.7 years[5,6].

59

60 Currently, mRNA platforms for cancer vaccines include conventional linear mRNA, circular
61 RNA (circRNA), and self-amplifying mRNA[7]. Conventional linear mRNA has already been
62 advanced to clinical application and represents the most mature mRNA vaccine technology to date.
63 Wesselhoeft et al. described the circRNA expression platform in 2018, which enables efficient and
64 stable protein expression via RNA circularization and internal ribosome entry site(IRES)-mediated
65 translation[8]. We previously engineered an optimized circRNA vaccine platform specifically for
66 cancer vaccine applications, which demonstrated superior antigen expression and immunogenicity

67 compared to conventional linear mRNA[9]. However, circRNA production requires complex
68 circularization and purification procedures, substantially complicating production workflows and
69 increasing costs[10,11]. The self-amplifying mRNA (saRNA) vaccines, encodes additional viral RNA
70 replication proteins to achieve *in vivo* RNA amplification and robust efficacy at low doses[12].
71 Nevertheless, because these vaccines produce a large amount of double-stranded RNA (dsRNA)
72 and express multiple heterologous viral proteins, they can induce systemic reactogenicity,
73 potentially compromising tolerability and therapeutic efficacy[13,14]. Furthermore, chemically
74 modified poly(A) mRNA[15] and multi-capped mRNA[16] strategies reported by Chen et al.
75 substantially enhance stability and translation but introduce additional manufacturing complexity
76 and tolerability concerns. To date, no existing platform achieves high potency without adding design
77 or production complexity.
78
79 By contrast, conventional linear mRNA remains the most readily manufactured vaccine
80 platform, with minimal intrinsic adverse effects [17]. However, linear mRNA's optimal translation
81 efficiency and stability requires two essential modifications: 5' capping[18,19] and modified
82 ribonucleotides[20,21]. These modifications also increase both production complexity and cost.
83 Circumventing the reliance of linear mRNA on 5' capping and ribonucleotide modifications could
84 enable the development of a streamlined vaccine platform that balances affordability,
85 manufacturability, and therapeutic efficacy. Studies have explored linear mRNA designs lacking a
86 5' cap structure[22–24], but they generally fail to provide sufficient protection to the mRNA's 5' end
87 and, therefore, are unlikely to serve as viable substitutes for traditional capped mRNA.

88

89 The mRNA 5' cap not only recruits eIF4E to facilitate translation initiation but also shields the
90 transcript's 5' terminus from XRN-1-mediated exonucleolytic decay [25,26], whereas incorporation of
91 modified ribonucleotides enhances mRNA stability[20,21]. A survey of the literature on viral and
92 eukaryotic mRNA metabolism reveals that these functions can, in principle, be conferred entirely
93 by RNA sequences and structural elements. For example, *Flavivirus* genomes harbor structured
94 elements that block XRN-1 to generate abundant subgenomic flaviviral RNAs (sfRNAs) during
95 infection[27,28], which could be repurposed to shield synthetic transcripts from exonucleolytic
96 digestion. Likewise, certain cellular RNA-binding proteins (RBPs), such as poly(A) binding
97 proteins (PABPs) and IGF2BP1, stabilize mRNAs. Specifically, PABPs binds and stabilizes the
98 poly(A) tail of most mRNAs[29], whereas IGF2BP1 associates with MYC and several other mRNAs
99 to enhance their half-lifes[30]. Integrating RBP-binding motifs is a viable strategy to further bolster
100 mRNA stability. Finally, IRES, such as our previously characterized EV-A IRES, can efficiently
101 drive cap-independent translation, effectively replacing the 5' cap's translational role[8,9].

102

103 In this study, we introduce a novel, entirely sequence-encoded linear cap-independent RNA
104 (LciRNA) platform that requires no 5' cap or ribonucleotide modifications by integrating the above-
105 mentioned elements. We began by using RNA secondary-structure modeling and luciferase
106 screening to identify an optimal XRN-1-resistant element from flaviviral sfRNA. This element was
107 fused to a PABP-binding sequence and an optimized *Enterovirus* A (EV-A) IRES variant, generating
108 LciRNA constructs that drive robust *in vivo* expression. Mechanistic analyses confirmed that these

109 elements both block XRN-1 decay and recruit endogenous RBPs, including PABP, IGF2BP1, and
110 YBX1, to stabilize transcripts. Additionally, LciRNA vaccines exhibit strong intrinsic adjuvant
111 activity, promoting dendritic cell maturation and proinflammatory cytokine release. Finally, we
112 assessed the safety profile of LciRNA in murine models and formulated LciRNA-based cancer
113 vaccines, which exhibited superior therapeutic efficacy in both B16F10 melanoma and HPV
114 associated tumor models.
115
116 **RESULTS**
117
118 **Engineering LciRNA with Flaviviral xrRNA and PABP Motif for Enhanced Stability and**
119 **Translation**
120 Previously, we characterized an optimized EV-A IRES (hereafter EV-A-S1) that drives efficient cap-
121 independent translation of target proteins[9]. Because a canonical 5' cap both recruits eIF4E and
122 protects the 5' end from XRN-1 mediated degradation[26], we sought RNA elements that could
123 similarly impede XRN-1 decay for cap-independent LciRNA. *Flavivirus* subgenomic RNAs
124 (sfRNAs) contain structured exoribonuclease-resistant RNA (xrRNA) and dumbbell elements to
125 stall XRN-1 progression[27,31,32]. Moreover, the mRNA 3' poly(A) tail recruits PABPs, which shield
126 transcripts from the 3' terminus[29], suggesting that integrating a PABP-binding motif may also
127 enhance 5'-end protection. We therefore designed LciRNA constructs that incorporate, at the 5' end,
128 an xrRNA/dumbbell element and a PABP-binding motif upstream of the EV-A-S1 IRES, and, at the
129 3' end, a 3' untranslated region (UTR) followed by a poly(A) tail (Figure 1A). To identify the most

130 effective XRN-1-resistant structure, we retrieved sfRNA sequences of five flaviviruses—Cellular
131 fusion agent virus (CFAV), Dengue virus (DENV), Usutu virus (USUV), Yellow fever virus (YFV),
132 and Zika virus (ZIKV)—from the NCBI virus database, referred to both published sfRNA structural
133 annotations[27] and RNAfold[33] predicted secondary structures (Figure S1), yielding 18 candidate
134 xrRNA/dumbbell sequences (Figure 1B).
135
136 We inserted each candidate motif at the 5' end of a Gaussia luciferase (Gluc) reporter LciRNA
137 carrying EV-A-S1 to enable rapid transcript stability screening via luminescence. All constructs
138 were *in vitro* transcribed without cap analogs or modified nucleotides and transfected into HEK293T
139 cells. After 48 h, luciferase assays revealed that UX1, DX1, ZX1, DD1, and DX2 significantly
140 outperformed the unprotected control (Figure 1C). Notably, UX1, derived from USUV, yielded the
141 highest expression and was therefore selected for further experiments.
142
143 Because untranslated regions modulate translation in circRNAs and capped mRNAs, we next
144 optimized all other untranslated regions including conventional 5' and 3' UTRs in LciRNA (Figure
145 1D). Incorporating a PABP motif between UX1 and EV-A-S1 yielded higher Gluc expression than
146 polyC motif, polyU motif, or no insert (Empty) (Figure 1E). Screening various 5' and 3' UTRs
147 revealed that human β-globin sequences at both sites provided maximal translation (Figure. 1F, 1G).
148 Accordingly, all subsequent LciRNA designs incorporate β-globin 5' and 3' UTRs.
149
150 **Ribonucleotide Modification and UX1's Structural Alteration Impair LciRNA Performance**

151 Ribonucleotide modifications often enhance mRNA stability and expression, so we evaluated their
152 impact on LciRNA. Prior studies have shown that N1-methyl-pseudouridine (m1Ψ) improves
153 mRNA stability and translational efficiency[21,34], m6A enhances circRNA translation[35], and N4-
154 acetylcytidine (N4-Ac-C) boosts IRES-mediated translation[36]. We thus incorporated 5–100% m6A,
155 m1Ψ, or N4-Ac-C into Gluc LciRNAs. Transfected into HEK293T cells, these modified RNAs
156 exhibited dose-dependent reductions in luciferase activity after 48 h (Figure 2A). This decline likely
157 reflects disruption of critical UX1 and IRES structures by noncanonical bases[37], underscoring that
158 LciRNA's function relies on precise folding and is incompatible with extensive ribonucleotide
159 modifications.
160
161 We subsequently examined whether UX1 structural modification could further enhance LciRNA
162 protection. Previous studies demonstrated that xrRNA blocking of XRN-1 is regulated by
163 pseudoknot length[38]. We therefore modeled UX1's structure using SHAPE-MaP (selective 2'-
164 hydroxyl acylation analyzed by primer extension and mutational profiling) and IPknot analysis,
165 revealing two pseudoknots, PK1 and PK2 (Figure 2B, S2A). Then, we generated UX1 mutants with
166 longer pseudoknots (Long-PK1, Long-PK2) or increased GC content in PK2 (mPK2) and assessed
167 their performance in Gluc LciRNA. Unexpectedly, all three mutants showed significantly
168 diminished expression levels compared with wild-type UX1 (Figure 2C), indicating that the native
169 88-nt UX1 sequence already achieves optimal XRN-1 resistance.
170
171 **Engineered LciRNA Outperforms m1Ψ-modified Capped mRNA in *in vivo* Persistence**

172 Building on our initial observation that coupling UX1 with a PABP-binding motif maximizes
173 LciRNA expression, we designated their combination the UPA protective sequence. We
174 hypothesized that tandem repeats of UPA could further enhance transcript stability. Accordingly, we
175 designed Gluc-encoding LciRNAs featuring one (UPA), two (2UPA), or three (3UPA) tandem UPA
176 units at the 5' terminus. These constructs were evaluated alongside unmodified (CAP) and m1Ψ-
177 modified (mCAP) Cap1-capped Gluc mRNAs, as well as uncapped RNAs containing only a 5'
178 PABP motif sequence (P-IRES) or the IRES alone. UPA-containing transcripts exhibited
179 significantly increased luciferase activity, although their expression at 48 h post-transfection
180 remained slightly below that of CleanCap-capped Cap1 mRNAs (Figure 2D). Notably, the 2UPA-
181 LciRNA achieved the highest expression, 10.5-fold higher than IRES-only control, demonstrating
182 that dual UPA repeats confer optimal protection.
183
184 To evaluate transcript expression dynamics, we transfected HeLa cells and sampled supernatants
185 daily for five days. The 2UPA and 3UPA LciRNAs sustained stable expression at levels equivalent
186 to capped mRNAs (Figure 2E). In contrast, single UPA LciRNA showed a modest decline, and the
187 IRES-only control dropped by over 10-fold each day; the PABP-IRES LciRNA showed only slight
188 improvement over the unprotected control (Figure 2E). These data confirm that the UPA motif
189 confers robust protection and that tandem UPA repeats restore cellular stability to match that of
190 Cap1-capped transcripts.
191

192 To evaluate *in vivo* expression, BALB/c mice were injected intramuscularly with SM102 LNP-
193 encapsulated UPA and 2UPA LciRNA encoding firefly luciferase (Fluc) as well as CAP and mCAP
194 Fluc mRNAs. Bioluminescence imaging over 120 h post-injection revealed that although 2UPA
195 LciRNA Fluc yielded lower luminescence within the first 24 h, its signal surpassed both mCAP Fluc
196 and CAP Fluc from 48 h to 120 h (Figure 2F, 2G, 2H). These findings demonstrate that 2UPA
197 LciRNA confers greater *in vivo* transcript stability than m1Ψ-modified capped mRNA. This *in vivo*
198 profile contrasts with our cell-culture results and underscores differences in mRNA translation and
199 turnover between immortalized cell lines and mammalian tissues. These differences are likely
200 driven by continuous proliferation and homogeneity in immortalized cells. Given that LciRNA
201 vaccines are intended for clinical application, *in vivo* expression kinetics may more accurately
202 predict therapeutic efficacy. In summary, our engineered LciRNA demonstrates superior *in vivo*
203 expression stability compared to m1Ψ-modified Cap1-capped mRNA, suggesting advantages for
204 cancer vaccine applications.
205
206 **UPA Sequence Stabilizes LciRNA Through XRN-1 Inhibition and RBP Binding**
207 The above results showed that incorporation of the UPA sequence endows uncapped LciRNA with
208 stability comparable to that of Cap1-capped mRNA. To elucidate the mechanism underlying UPA-
209 mediated stabilization, we assessed its capacity to inhibit XRN-1 mediated degradation and to
210 recruit intracellular RBPs. In an *in vitro* XRN-1 degradation assay (Figure 3A), the uncapped and
211 unprotected RNA (IRES) was completely degraded after 2 h of XRN-1 treatment, whereas UPA and
212 2UPA LciRNAs as well as capped mRNA (CAP) remained largely intact (Figure 3B). Consistent

213 with Gluc expression results, 2UPA conferred stronger protection than a single UPA, demonstrating
214 that UPA impedes XRN-1 digestion of LciRNA and that tandem duplication further potentiates this
215 effect.
216
217 We next sought UPA-binding proteins by fusing the UPA sequence to a streptavidin aptamer (SA)
218 [39] and performing RNA pull-down with streptavidin-coated beads(Figure 3C). HeLa cell lysates
219 were incubated with beads bearing either the UPA–SA aptamer fusion or SA aptamer alone, and
220 bound proteins were resolved by SDS–PAGE (Figure 3D). Mass spectrometry, western blotting, and
221 RNA immunoprecipitation analyses identified YBX1, PABPC1, ILF2, ILF3, IGF2BP1, and PKR as
222 UPA-specific interactors in the cytoplasm (Figure 3E, 3F, S2B). Notably, ILF2, ILF3, and PKR are
223 immune regulatory proteins, suggesting UPA's role in immune signaling [40–44]. PABPC1, which binds
224 poly(A) tails to stabilize transcripts and enhance translation, likely reinforces LciRNA stability and
225 translational efficiency via the PABP motif in UPA. Similarly, YBX1 and IGF2BP1 are well-
226 established RBPs that promote mRNA stability [30,45,46], and their association with UPA may further
227 elevate LciRNA stability.
228
229 To assess each RBP's role in LciRNA expression, we performed siRNA-mediated knockdown
230 (excluding PABPC1 to preserve 3' tail integrity) in HeLa cells (Fugure 3G). We then transfected
231 UPA-Gluc LciRNA, IRES-Gluc RNA, and capped Gluc mRNA and measured Gluc activity. PKR
232 depletion significantly increased expression of all three RNA constructs (Fugure 3H), likely due to
233 relief of PKR mediated eIF2α phosphorylation and global translational repression[41,43,47]. In contrast,

234 knockdown of ILF2 or ILF3 reduced expression of all three RNAs (Fugure 3I), consistent with their
235 reported roles in mitosis and effects on cell viability[48,49]. Notably, silencing IGF2BP1 or YBX1
236 preferentially decreased UPA-LciRNA expression without affecting the other RNAs (Figure 3J).
237 Given the established RNA-stabilizing functions of IGF2BP1 and YBX1[30,45,46], these findings
238 indicate that the UPA motif enhances LciRNA stability not only by blocking XRN-1 mediated decay
239 but also via recruitment of IGF2BP1, YBX1, and PABPC1.
240
241 **Self-Adjuvanting LciRNA Drives PRR-Mediated DC Maturation with Minimal Toxicity**
242 The ultimate goal of a cancer vaccine is to elicit potent, tumor-specific immune responses, which
243 require both efficient antigen expression and the vaccine's intrinsic or adjuvant mediated
244 immunostimulatory capacity[50,51]. Unlike conventional capped mRNA, LciRNA possesses a 5'-
245 triphosphate moiety that is recognized by pattern recognition receptors such as RIG-I, thereby
246 potently triggering inflammatory signaling [52]. Its viral-derived IRES contains extended stem-loop
247 structures that may be sensed by protein kinase R (PKR) and toll-like receptors (TLRs), activating
248 downstream innate immune cascades[53–55]. Furthermore, the UPA's interactions with PKR, ILF2 and
249 ILF3 potentially enhance cellular recognition of LciRNA[40–44,56]. Collectively, these features suggest
250 that LciRNA engages multiple pattern recognition receptors (PRRs) to initiate innate immune
251 pathways, conferring a self-adjuvant effect that can amplify adaptive antitumor immunity.
252
253 To assess the potential immunostimulatory ability of LciRNA vaccines, mouse bone marrow
254 derived dendritic cells (BMDCs) were transfected with Fluc-encoding LciRNAs (UPA-Fluc, 2UPA-

255 Fluc) or capped Fluc mRNAs (CAP-Fluc, mCAP-Fluc). At 24 h post-transfection, total RNA was
256 harvested for quantitative RT-PCR and RNA sequencing. qRT-PCR analysis revealed that BMDCs
257 transfected with either LciRNA construct upregulated MHC-I, the co-stimulatory molecules CD40,
258 CD80, and CD86, and the proinflammatory cytokines IFN-α, IFN-β, and IL-6, to a significantly
259 greater extent than cells receiving capped mRNA; only unmodified CAP-Fluc induced modest
260 increases in CD40, IL-6, and IFN-β (Figure 4A). Transcriptomic analysis demonstrated that
261 LciRNA strongly activated gene sets associated with antigen processing and presentation, RIG-I
262 and TLR signaling, type I interferon response, and inflammatory cytokine production (Figure 4B,
263 4C). Further examination of PRR-induced dendritic cell (DC) maturation gene signatures[57] revealed
264 near-complete concordance between genes upregulated by LciRNA and canonical PRR-upregulated
265 genes (Figure S3A), indicating that LciRNA drives DC maturation via PRR engagement. Moreover,
266 LciRNA markedly increased the expression of T cell co-stimulatory molecules, proinflammatory
267 chemokines (Cxcl9, Cxcl10), and cytokines (Il6, Il12, Il15, Ifna1, Ifnb1) (Figure S3B). Collectively,
268 these data confirm that LciRNA potently activates PRR signaling, promotes DC maturation, and
269 induces proinflammatory chemokine and cytokine expression, supporting its strong self-adjuvant
270 capacity to enhance antitumor immune responses.
271
272 To evaluate potential *in vivo* toxicity of LciRNA vaccines, we formulated SM102 LNPs
273 encapsulating UPA-E6E7 LciRNA, 2UPA-E6E7 LciRNA, or m1Ψ-modified CleanCap-E6E7
274 mRNA, and administered 5 μg RNA intramuscularly to C57BL/6 mice, followed by a booster dose
275 one week later. Body weight and serum alanine aminotransferase (ALT) and aspartate

276 aminotransferase (AST) levels were measured before immunization and seven days after each dose.
277 No vaccinated group exhibited significant deviations in body weight compared with untreated
278 controls (Figure 4D). Similarly, ALT and AST levels remained comparable to baseline and those of
279 untreated controls (Figure 4E, 4F). Two weeks after the booster dose, histopathological examination
280 of heart, liver, spleen, lung, and kidney via H&E staining revealed no vaccine-related lesions (Figure
281 4G). These findings demonstrate that LciRNA vaccines are well tolerated in mice at a dosing
282 regimen equivalent to 1 mg per dose in humans.
283
284 **LciRNA Vaccination Provokes Potent Tumor-Specific T Cell Responses and Controls B16F10-**
285 **OVA Melanoma Growth**
286 To evaluate therapeutic efficacy of LciRNA-based cancer vaccines, we established an ovalbumin-
287 expressing B16F10 (B16F10-OVA) melanoma model in C57BL/6 mice. On day 3 and 10 post tumor
288 inoculation, mice received intramuscular doses of 3 μg UPA-OVA LciRNA, 2UPA-OVA LciRNA,
289 m1Ψ-modified capped mCAP-OVA mRNA, or m1Ψ-modified capped Fluc control mRNA (Figure
290 5A). Tumor growth monitoring revealed that all OVA-targeting vaccines significantly inhibited
291 tumor growth compared with mCAP-Fluc, with the 2UPA-OVA cohort exhibiting the most
292 pronounced inhibition (Figure 5B). On day 20, excised tumors from UPA-OVA and 2UPA-OVA
293 groups were markedly smaller, and complete tumor regression occurred in 3/6 mice per group,
294 versus 1/6 in the mCAP-OVA group (Figure 5C, S4B). Body weights remained stable across all
295 groups, indicating favorable tolerability (Figure S4A). These results demonstrate that LciRNA
296 vaccines provide superior antitumor efficacy over m1Ψ-modified capped mRNA in mouse

297 melanoma model.

298

299 To evaluate antigen-specific T cell responses, peripheral blood mononuclear cells (PBMCs) were
300 collected one week after the booster and stained with OVA (SIINFEKL) Tetramer. FACS analysis
301 revealed that UPA-OVA, 2UPA-OVA, and mCAP-OVA vaccines induced 15.8%, 22.9%, and 19.1%
302 OVA-specific CD8+ T cells on average, respectively, versus 0.7% in control group (Figure 5D, 5E),
303 with 2UPA-OVA eliciting the strongest response. On day 20, spleens and tumors were harvested to
304 further characterize systematic and intratumoral T cell responses. Splenocytes restimulated ex vivo
305 with OVA mRNA exhibited the highest frequency of IFN-γ^+ $CD8^+$ T cells in the 2UPA-OVA group
306 compared to UPA-OVA and mCAP-OVA (Figure 5F, S4C). Analysis of tumor-infiltrating
307 lymphocytes showed that both UPA-OVA and 2UPA-OVA significantly increased the proportion of
308 OVA-specific CD8+ T cells (Figure 5G) and total CD4+ and CD8+ T cell infiltration (Figure 5H,
309 5I) relative to mCAP-OVA and control. These findings suggest that LciRNA vaccines convert
310 immunologically "cold" tumors into "hot" tumors by enhancing T cell infiltration. Collectively, the
311 2UPA-OVA LciRNA vaccine demonstrated the most robust antitumor efficacy and T cell induction,
312 while UPA-OVA matched mCAP-OVA in systematic T cell response but achieved greater tumor
313 control, presumably owing to its self-adjuvant activity that enhanced T cell infiltration.

314

315 **Effective Clearance of HPV associated Tumors by LciRNA-Based Therapeutic Vaccination**

316 Human papillomavirus (HPV) infection is etiologically linked to cervical and oropharyngeal cancers,
317 in which tumor cells commonly express the viral oncoproteins E6 and E7[58,59]. Therefore, the E6 and

318 E7 proteins serve as ideal target antigens for HPV-associated malignancies. To assess the therapeutic
319 potential of our HPV E6E7 LciRNA vaccines, we established an HPV-associated tumor model by
320 subcutaneously injecting C57BL/6 mice with HPV-E6/E7–expressing TC-1 cells. When tumors
321 reached ~50 mm^3 on day 9, mice received intramuscular injections of 3 μg UPA-E6E7 LciRNA,
322 2UPA-E6E7 LciRNA, m1Ψ-modified capped mCAP-E6E7 mRNA, or m1Ψ-modified capped Fluc
323 control mRNA (mCAP-Fluc) (Figure 6A). Following two immunizations, all three E6E7 vaccine
324 groups exhibited continuous tumor regression, whereas tumors in control mice progressed rapidly
325 (Figure 6B, S6C). On day 23, mice were photographed, showing significantly smaller tumors in the
326 UPA-E6E7 and 2UPA-E6E7 groups (Figure S6B). Survival analysis demonstrated that all mice in
327 the three E6E7 vaccine groups survived beyond the 40-day observation period, while complete
328 tumor regression was achieved by day 33 in mice vaccinated with UPA-E6E7 or 2UPA-E6E7,
329 compared to day 40 for mCAP-E6E7 (Figure 6C, S6C). These results indicate that the LciRNA
330 vaccines achieved more rapid tumor eradication than m1Ψ-modified capped mRNA.
331
332 PBMCs were harvested one week after the booster dose and restimulated with E6/E7 peptides.
333 FACS results showed high frequencies of IFN-γ^+ T cells in all E6E7 vaccine groups (mean IFN-γ^+
334 $CD8^+$ T cells proportions: UPA-E6E7 9.6%; 2UPA-E6E7 15.5%; mCAP-E6E7 13.6%; mCAP-Fluc
335 0.1%) (Figure 6D, 6E), with 2UPA-E6E7 eliciting the strongest response. On day 40, splenocytes
336 restimulated ex vivo with mCAP-E6E7 mRNA again showed the highest frequency of IFN-γ^+ $CD8^+$
337 T cells in the 2UPA-E6E7 group, significantly exceeding that of the mCAP-E6E7 cohort (Figure 6F,
338 S7A). Collectively, these results demonstrate that 2UPA-E6E7 LciRNA elicit robust and durable

339 antigen-specific $CD8^+$ T-cell responses that correlate with their superior antitumor efficacy.

340

341

342 **DISCUSSION**

343

344 We engineered a streamlined, cap-independent LciRNA vaccine platform by combining the USUV
345 sfRNA-derived UX1 sequence with a PABP motif to create the UPA protective element, and pairing
346 it with the cap-independent EV-A-S1 IRES. Unlike conventional capped mRNA, incorporation of
347 modified ribonucleotides into LciRNA markedly reduced its expression. In contrast, tandem
348 duplication of UPA (2UPA) yielded an unmodified LciRNA whose *in vivo* stability in mice
349 surpassed that of m1Ψ-modified cap1 mRNA. Mechanistic analysis revealed that UPA not only
350 blocks XRN-1 mediated decay but also recruits the stabilizing RBPs PABPC1, IGF2BP1, and YBX1
351 to further enhance LciRNA stability. Transcriptome profiling of BMDCs transfected with LciRNA
352 demonstrated potent activation of PRRs signaling, enhanced dendritic cell maturation, and
353 upregulation of antigen-presentation and proinflammatory cytokine expression, indicating a strong
354 intrinsic self-adjuvant effect. Safety evaluation by monitoring body weight, serum ALT and AST
355 levels, and histopathological analysis confirmed that LciRNA vaccine is well tolerated in mice.
356 Finally, in both B16F10 melanoma and HPV-associated tumor models, LciRNA-based vaccines
357 elicited superior immunogenicity and tumor control compared with traditional capped, modified
358 mRNA vaccines.

359

360 Comparing with existing mRNA vaccine platforms, LciRNA relies solely on functional RNA
361 sequences—no exogenous proteins, complex processing, or modified ribonucleotides—simplifying
362 production while outperforming conventional linear mRNA in both expression and immunogenicity,
363 thus defining a novel type of mRNA vaccine platform. Previously, several studies also explored
364 uncapped linear RNA designs: Two groups replaced the 5' cap with a single IRES, yielding an
365 uncapped RNA successfully expressed in cells and *in vivo*[22,23]. However, our results show that
366 uncapped RNA without any protection decays rapidly (Figure 2D, 2E). Similarly, another group
367 proposed a hairpin-protected uncapped RNA encoding the influenza HA antigen, which successfully
368 elicited antibody response[24]. We found that the artificial hairpin sequence did confer modest
369 protection to the uncapped RNA, but its stability remained markedly lower than that of capped
370 mRNA or LciRNA (data not shown). Given that XRN-1 is capable of resolving complex secondary
371 structures[60,61], simple hairpin structures are unlikely to offer sufficient protection against its
372 degradation. By contrast, viral xrRNAs adopt a precise three-dimensional embrace[31,38], that blocks
373 the XRN-1 active site, effectively preventing RNA unfolding and degradation. Our findings provide
374 compelling evidence that tandem duplication of UX1 with a PABP motif (2UPA) substantially
375 stabilizes LciRNA *in vivo*, surpassing the performance of capped mRNA. Moving forward, the
376 LciRNA platform can be further optimized by incorporating additional 3'-end protective elements
377 or refining the UPA and IRES sequences to boost functionality while reducing overall transcript
378 length.
379

380 Furthermore, LciRNA exhibits intrinsic immunostimulatory activity, making it an ideal tumor
381 vaccine platform. In dendritic cells, LciRNA engages multiple pattern recognition receptors, leading
382 to enhanced antigen presentation and increased chemokine and cytokine secretion, which in turn
383 drive tumor-specific T cell activation and expansion (Figure 7). In a murine melanoma model,
384 LciRNA also augmented intratumoral T cell infiltration, potentially remodeling the tumor immune
385 microenvironment toward an active state. Solid tumors frequently establish immunosuppressive
386 microenvironments characterized by poor immune cell infiltration, which correlates with adverse
387 clinical outcomes[62]. Although combining mRNA vaccines with immune checkpoint inhibitors has
388 yielded promising results in recent trials[4–6], these strategies depend on capped mRNA with
389 inherently weak innate immunogenicity, restricting their ability to overcome tumor-induced
390 immunosuppression. In contrast, our LciRNA platform leverages intrinsic self-adjuvant activity to
391 provoke strong proinflammatory signaling, remodel the tumor microenvironment, and enhance
392 therapeutic efficacy both as monotherapy and in combination regimens.
393
394 The immunostimulatory capacity likely derives from three features of LciRNA: its 5'-
395 triphosphate moiety, which is recognized by RIG-I[52]; the UPA sequence, which binds ILF3 in the
396 cytoplasm and relieves its nuclear suppression of dendritic cell maturation and proinflammatory
397 gene expression in DCs[56]; and the viral-derived IRES, whose extended stem–loop structures could
398 be sensed by PKR and TLRs[53–55]. Together, these features enable multi-PRR engagement and relief
399 of ILF3-mediated immune suppression, robustly inducing downstream immune gene activation

400 (Figure 7). Future mechanistic and translational exploration of LciRNA's adjuvanticity could
401 maximize its therapeutic potential in cancer immunotherapy.
402
403 Nonetheless, this study has several limitations. First, a comprehensive safety assessment of
404 LciRNA will require long-term and higher-dose studies, additional animal species, and more
405 physiological readouts. Second, while we demonstrated specific interactions between the UPA motif
406 and ILF2, ILF3, and PKR, the downstream biological effects are uncharacterized. Notably, ILF3
407 has established roles in mRNA stability and immune suppression[42,56], while ILF2 mainly contributes
408 to cell cycle control and apoptosis[44,63,64]. Their association with UPA may influence LciRNA's
409 immunogenicity and tolerability. Additionally, PKR knockdown enhanced LciRNA translation,
410 suggesting that PKR both restricts expression and promotes immune activation. Future studies must
411 balance these functions to optimize LciRNA's therapeutic profile.
412
413 In summary, LciRNA obviates capping and ribonucleotide modifications, simplifying
414 manufacture and reducing cost while offering enhanced stability and intrinsic adjuvant activity. By
415 engaging diverse PRRs and promoting DC maturation, LciRNA enhances T cell infiltration in "cold"
416 tumors, expanding the therapeutic reach of RNA vaccines. As a fully sequence-encoded, fourth-
417 generation mRNA vaccine platform, LciRNA establishes a new design paradigm for future RNA
418 vaccines.
419
420

421 **MATERIALS AND METHODS**

422 **Molecular cloning**

423 All the LciRNA template sequences were cloned into pUC57 plasmid through seamless cloning.
424 The Cloning Kit for mRNA Template (Takara Bio) was used to construct all the capped mRNA
425 templates. DNA fragments were synthesized by Genewitz (Suzhou, China) and amplified by PCR.
426 ClonExpress II One Step Cloning Kit form Vazyme (Nanjing, China) were used for seamless cloning.
427 All the related sequences are provided in Table S1 and Table S2.

428

429 **LciRNA and capped mRNA synthesis**

430 For both types of RNAs, the DNA templates for IVT were first amplified by PCR using
431 2×AdvanceFast PCR Master Mix (Yeasen, Shanghai) and primers with T7 promoter and 120nt
432 poly(T) (to add 120nt poly(A) tail during transcription). The LciRNAs were synthesized using T7
433 High Yield RNA Synthesis Kit (Yeasen, Shanghai) without addition of any cap analog or modified
434 ribonucleotides. The modified LciRNAs were synthesized using T7 High Yield RNA Synthesis Kit
435 (Yeasen, Shanghai) with indicated proportion of modified ribonucleotide added (m6A, m1Ψ, or N4-
436 Ac-C from Syngenebio), but without addition of any cap analog. The capped mRNAs were
437 synthesized using T7 High Yield RNA Synthesis Kit (Yeasen, Shanghai) with CleanCap Reagent
438 AG (TriLink) and m1Ψ (Syngenebio) added co-transcriptionally. Both types of RNAs were
439 subsequently treated with DNase I at 37℃ for 20 mins, and purified using GeneJET RNA
440 Purification Kit (Thermofisher). Final RNA products were analyzed by 2% agarose gel or capillary
441 electrophoresis.

442

443 **Luciferase reporter assay**

444 For gaussia luciferase assay, cells were cultured in 96 well plate at the density of 5,000 cells per
445 well. The next day, mRNAs were transfected with CALNP mRNA *in vitro* reagent (D-nano, Beijing)
446 at 50ng per well according to manufacturer's instruction. 24 hours later, 30μL cell culture medium
447 was taken from each well, and luminescence counts were measured using Gaussia Luciferase
448 Reporter Gene Assay Kit (Beyotime) according to manufacturer's instruction.

449

450 **SHAPE-MaP analysis of UX1 structure.**

451 The UX1 RNA structure was analyzed by SHAPE-MaP method reported by Smola et al [35] with
452 some modifications as described by our previous study[9].

453

454 **siRNA knockdown**

455 HEK293T cells were cultured in 24 well plates at 100,000 cells per well. siRNAs targeting
456 corresponding proteins were transfected at 30pmol per well with Hieff Trans siRNA/miRNA reagent
457 (Yeasen). 48 hours later, total RNAs of three of the replicate wells were extracted and assayed by
458 RT-qPCR to analysis knockdown efficiency. mRNAs were transfected into the other three replicates,
459 at 200ng per well with TransIT-mRNA Transfection Kit (Mirusbio). 24 hours later, 30μL cell culture
460 medium was taken from each well to measure gaussia luciferase signal. siRNA sequences were
461 synthesized by Hipobio (Huzhou, Zhejiang) and provided in Table S3.

462

463 **LNP encapsulation of RNA**

464 All RNAs used in injection of mice were encapsulated by the SM102 LNP mix using GenNano-
465 E0021 cancer vaccine kit (Micro&Nano, Shanghai) according to manufacturer's instruction. Qubit
466 2.0 (Invitrogen) and Qubit RNA HS (Invitrogen) were used to determine the RNA concentration in
467 the RNA-LNP vaccine (2% Triton X-100 was added to disrupt the RNA-LNP sample).

468

469 ***In vivo* bioluminescence imaging in mice**

470 The Fluc RNA-LNP (5 μg RNA per mouse) was intramuscularly injected into the right thigh of the
471 mice. At indicated time points, 200 μL of D-luciferin potassium salt (Meilun Biology, Dalian) was
472 administered per mouse. Fluorescence imaging was performed and analyzed using the IVIS *in vivo*
473 imaging system (PerkinElmer) within 10–30 min after substrate injection.

474

475 **XRN-1 Digestion Assay**

476 For the XRN-1 digestion assay, 2 μg of RNA was first denatured at 70 °C for 2 min and immediately
477 placed on ice. The RNA was then refolded in a 20 μL reaction containing 1× NEBuffer 3 (NEB) and
478 1 U/μL RNase Inhibitor murine (Vazyme) at 37 °C for 10 min. Subsequently, 1 U of XRN-1 (NEB)
479 and 10 U of RppH (NEB) were added, followed by incubation at 37 °C for 2 h. After digestion, 5
480 μL of the reaction mixture was mixed with 5 μL of 2× RNA loading buffer, heat-denatured at 95 °C
481 for 1 min, and analyzed alongside an equal amount of undigested RNA using 2% agarose gel
482 electrophoresis.

483

484 **RNA pull-down assay**

485 Streptavidin-coated magnetic beads (QuarAcces, Diying, Shanghai) were equilibrated at room
486 temperature for 30 min, washed twice with Solution A (0.1 M NaOH, 0.05 M NaCl in DEPC-treated
487 H_2O) and once with Solution B (0.05 M NaCl in DEPC-treated H_2O), then resuspended in Solution
488 B. In parallel, 30 μg of streptavidin-aptamer–tagged RNA was denatured at 56 °C for 5 min in
489 RNase-free water, refolded in annealing buffer (100 mM Tris-HCl pH 7.5, 300 mM NaCl, 3 mM
490 $MgCl_2$, 2 U/μL murine RNase inhibitor) at 37 °C for 10 min followed by 5 min at room temperature,
491 and incubated with the pretreated beads for 10 min at room temperature and then rotated for 2 h at
492 4 °C. HeLa cell lysates were cleared by centrifugation (15 000 × g, 15 min, 4 °C), pre-adsorbed with
493 empty beads for 30 min at 4 °C, and subsequently incubated with the RNA-bound beads in the
494 presence of 1.5 mM $MgCl_2$ for 4 h at 4 °C. Beads were washed six times with NT2 buffer (50 mM
495 Tris-HCl pH 7.5, 150 mM NaCl, 1.5 mM $MgCl_2$), and proteins were eluted in 1× SDS loading buffer
496 by boiling at 100 °C for 10 min. Finally, eluates were resolved on a 10% SDS-PAGE gel (18 × 16
497 cm) at 40 V, silver-stained (Beyotime Biotechnology Fast Silver Stain Kit), and differentially visible
498 bands excised for mass spectrometry analysis.

499

500 **Western blotting**

501 Pull-down protein samples and 5% Hela cell lysate input were separated on a 10% sodium dodecyl
502 sulfate-polyacrylamide gel and transferred on to a nitrocellulose membrane (Bio-Rad, Hercules, CA,
503 USA). The membrane was next blocked with 5% non-fat milk and incubated with antibodies of
504 indicated proteins or β-Actin antibody. The protein bands were detected using a Tanon 5200

505 Chemiluminescent Imaging System (Tanon, Shanghai, China) with Omni-ECL reagents (Epizyme
506 Biotech, China). Antibodys used in western blotting were YBX1 (84993-4-RR, Proteintech),
507 PABPC1 (66809-1-Ig, Proteintech), ILF2 (67685-1-Ig, Proteintech), ILF3 (68213-1-Ig, Proteintech),
508 IGF2BP1 (22803-1-AP, Proteintech), EIF2AK2 (66646-1-Ig, Proteintech), DDX3X (67915-1-Ig,
509 Proteintech), HNRNPR (29980-1-AP, Proteintech), β-Actin (66009-1-Ig, Proteintech).
510
511 **RNA immunoprecipitation assay**
512 2×5μg UPA-SA aptamer RNA was transfected into two 10cm plates of Hela cells 24 hours before
513 harvesting the cells. Cells were harvested by scraping in 1 mL PBS, and pelleted by centrifugation
514 at 800 ×g for 5 min at 4°C. The cell pellet was lysed in 800 μL RIP lysis buffer supplemented with
515 RNase inhibitor (Vazyme) and protease inhibitor (MedChemExpress), and incubated on ice for 30
516 min before storage at −80°C. For immunoprecipitation, 50 μL protein G magnetic beads per sample
517 were washed twice with NT2 buffer, incubated with 5 μg target antibody or control IgG in 200 μL
518 NT2 buffer for 1 h at room temperature with rotation, washed again, and resuspended in 500 μL ice-
519 cold NT2 buffer. Cell lysates were cleared by centrifugation (15,000 ×g, 20 min, 4°C), and 100 μL
520 supernatant was incubated overnight at 4°C with antibody-bound beads in 900 μL precipitation
521 buffer (NT2 buffer with 35 μL 0.5 M EDTA and 5 μL RNase inhibitor). Beads were washed six
522 times with NT2 buffer, and 50 μL was reserved for Western blot validation. RNA was extracted
523 using TRIzol (Invitrogen), reverse transcribed, and analyzed by qPCR to assess enrichment.
524 Antibodys used in RIP assay were Rabbit IgG (30000-0-AP, Proteintech), Mouse IgG (B900620,
525 Proteintech), YBX1 (84993-4-RR, Proteintech), PABPC1 (66809-1-Ig, Proteintech), ILF2 (67685-

526 1-Ig, Proteintech), ILF3 (68213-1-Ig, Proteintech), IGF2BP1 (22803-1-AP, Proteintech), EIF2AK2
527 (66646-1-Ig, Proteintech), DDX3X (67915-1-Ig, Proteintech), HNRNPR (29980-1-AP, Proteintech).
528
529 **RNA extraction and RT-qPCR**
530 Total RNA was extracted using TRIzol (Invitrogen) following the manufacturer's instructions.
531 cDNA was synthesized from using Evo M-MLV Reverse Transcription Kit (Accurate Biotechnology,
532 Huan) following the manufacturer's instructions. mRNA levels were quantified using SYBR Green
533 Premix Pro Taq HS qPCR Kit (Accurate Biotechnology, Huan). Primer sequences are provided in
534 Table S4. All qPCR reactions were performed on QuantStudio 5 Real-Time PCR System (Applied
535 Biosystems).
536
537 **siRNA knockdown**
538 Hela cells were cultured in 24 well plates at 100,000 cells per well. siRNAs targeting corresponding
539 proteins were transfected at 30pmol per well with Hieff Trans siRNA/miRNA reagent (Yeasen). 48
540 hours later, total RNAs of three of the replicate wells were extracted and assayed by RT-qPCR to
541 analysis knockdown efficiency. mRNAs were transfected into the other three replicates, at 200ng
542 per well using CALNP mRNA *in vitro* reagent (D-nano, Beijing). 24 hours later, 30μL cell culture
543 medium was taken from each well to measure gaussia luciferase signal. siRNA sequences were
544 synthesized by Hipobio (Huzhou, Zhejiang) and provided in Table S4.
545
546 **BMDC stimulation asssay**

547 BMDCs were generated with the method reported by Lutz et al. [66] For BMDC stimulation assay,
548 BMDCs were cultured in 24 well plates at 250,000 cells per well with mGM-CSF (Peprotech)
549 added to 4ng/mL. 6 hours later, 800ng indicated RNAs or transfection control were transfected into
550 each well using CALNP mRNA *in vitro* reagent (D-nano, Beijing). 24 hours later, total RNAs were
551 extracted and analyzed by RT-qPCR as well as RNA-seq.
552
553 **RNA-Seq Analysis**
554 Total RNA from BMDC samples were isolated using TRIzol (Invitrogen) following the
555 manufacturer's instructions. To eliminate DNA contamination, total RNAs were treated with DNase
556 I (Yeason). The RNA-seq libraries were prepared by using SMARTer Stranded Total RNA-Seq Kit
557 - Pico Input Mammalian (Yeason). Quality control was performed using Qubit (Thermo Fisher
558 Scientific, USA) and Qsep100 (BiOptic, China) before the libraries were sequenced on the BGI
559 DNBSEQ-T7 Sequencing Platform using a 150 bp paired-end run. The RNA-seq data sequencing
560 reads were aligned to the reference genome (Genome Reference Consortium GRCh38) using
561 the spliced read aligner STAR, which was provided with the Ensembl human genome assembly. The
562 gene expression matrix was obtained by featureCounts and be normalized by TPM for downstream
563 analysis.
564 For data analysis, genes with $|\log_2 FC| > 1$ and adjusted p-value (FDR) < 0.05 were classified as
565 differentially expressed (DEGs). Gene Set Enrichment Analysis (GSEA) was performed using the
566 clusterProfiler v4.2.2 R package. DEGs were ranked by $\log_2 FC$ values and tested against the
567 Molecular Signatures Database (MSigDB). Pattern recognition receptor (PRR)-related genes were

568 curated from literature-defined sets encompassing Toll-like receptors (TLRs), NOD-like receptors
569 (NLRs), RIG-I-like receptors (RLRs), and C-type lectins (CLRs). Heatmaps were generated using
570 the pheatmap v1.0.12 R package: DEG expression values were transformed to z-scores by row, and
571 visualized with diverging color gradients.
572
573 **Animal model**
574 Male C57BL/6 and BALB/c mice aged between 6-8 weeks were purchased from Biocytogen
575 (Beijing, China).
576 For in vivo bioluminescence assay, BALB/c mice were injected with 100μL Fluc RNA-LNPs (5μg
577 RNA per mouse) via intramuscular injection to the right thigh. At the indicated time points, 200 μL
578 D-luciferin potassium salt solution (15mg/mL) was injected to each mouse through intraperitoneal
579 injection. In vivo luminescence signal was measured using an IVIS Spectrum system (PerkinElmer)
580 10 min later. Data were analyzed using Living image software.
581 For serum ALT and AST evaluation, mouse blood was collected at the indicated time points, and
582 kept at room temperature for 60 min for coagulation. Serum samples were collected through
583 centrifugation at 3000 rpm/min under 4°C. Then, serum samples were sent to Fudan University
584 Laboratory Animal Center for analysis using ADVIA XPT (SIEMENS). For HE-staining of mouse
585 tissue, after euthanizing the mice, organ samples were collected, fixed and paraffin-embedded,
586 sectioned, and stained for H&E (Servicebio).
587 For the murine melanoma model, $1x10^5$ B16F10-OVA cells in 200ul RPMI 1640 medium (without
588 fetal bovine serum) were subcutaneously injected into the right flank of C57BL/6N mice. For the

589 HPV associated TC-1 model, $1x10^5$ TC-1 cells in 200ul RPMI 1640 medium (without fetal bovine
590 serum) were subcutaneously injected into the right flank of C57BL/6N mice. Mice body weight and
591 tumors were measured twice every week. Tumor volumes were determined by using the formula
592 volume = (length × $width^2$)/2 (L: largest diameter of the tumor; W: smallest diameter of the tumor).
593 For immunization, the mice were vaccinated with 100μL RNA-LNPs (3μg RNA per dose) via
594 intramuscular injection to the right thigh. All experiments were performed in accordance with
595 protocols approved by Fudan University Experimental Animal Care Commission.
596
597 **Flow cytometry analysis**
598 For OVA (SIINFEKL) Tetramer staining, PBMCs was separated by Mouse 1× Lymphocyte
599 Separation Medium (DAKEWE, Shenzhen) according to the manufacturer's instruction. Cells were
600 then stained with Fixable Viability Dye eFluor 450 (65-0863-14, eBioscience), anti-CD3 (APC-
601 65077, Proteintech), anti-CD8a (FITC-65069, Proteintech), H-2Kb&B2M&OVA (SIINFEKL)
602 Tetramer (PE, ACROBiosystems), and analyzed by CytoFLEX Flow Cytometer (Beckman).
603 For intratumoral T cell staining, tumor tissues were dissected into 1–2 mm^3 fragments in ice-cold
604 RPMI 1640 medium (10% FBS). Samples were digested in a cocktail of 1 mg/mL collagenase IV
605 (Yeasen) and 100 U/mL DNase I (Yeasen) for 30 min at 37°C with constant agitation (200 rpm).
606 Cells were then stained with Fixable Viability Dye eFluor 450 (65-0863-14, eBioscience), anti-CD3
607 (APC-65077, Proteintech), anti-CD8a (FITC-65069, Proteintech), anti-mouse CD4（PE-CY7,
608 Biolegend）, H-2Kb&B2M&OVA (SIINFEKL) Tetramer (PE, ACROBiosystems) , and analyzed
609 by CytoFLEX Flow Cytometer (Beckman).

610 For intra-cellular IFNγ staining, PBMCs or splenocytes was separated by Mouse 1× Lymphocyte
611 Separation Medium (DAKEWE, Shenzhen) according to the manufacturer's instruction. Cells were
612 then stained with Fixable Viability Dye eFluor 450 (65-0863-14, eBioscience), anti-CD3 (APC-
613 65077, Proteintech), anti-CD8a at 4°C for 30min. Subsequently, cells were fixed and permeabilized
614 with Intracellular Fixation and Permeabilization Buffer Set (eBioscience) according to the
615 manufacturer's instruction, and stained with anti-IFNγ (PE, Biolegend) at room temperature for
616 20min, and analyzed by CytoFLEX Flow Cytometer (Beckman).
617
618 **Statistical analysis**
619 All data in this study were analyzed via Graphpad Prism and presented as mean (SD) unless
620 otherwise indicated. Two-tailed unpaired Student's t-test was used to compare two groups. One-way
621 ANOVA tests were used to compare more than two groups. For survival curves, the data was
622 performed via Kaplan-Meier analysis. *$P < 0.05$ was considered statistically significant. **$P < 0.01$,
623 ***$P < 0.001$ and ****$P < 0.0001$ were considered highly significant. ns, not significant.
624
625 **ABBREVIATIONS**
626 mRNA: messenger RNA; LciRNA: Linear cap-independent RNA; circRNA: circular RNA; saRNA:
627 self-amplifying mRNA; dsRNA: double-stranded RNA; IRES: internal ribosome entry site; DC:
628 dendritic cells; RBPs: RNA-binding proteins; sfRNA: subgenomic flaviviral RNA; PABP: poly(A)-
629 binding protein; GLuc: Gaussia luciferase; FLuc: firefly luciferase; EV-A: *Enterovirus* A; xrRNA:
630 exoribonuclease-resistant RNA; m1Ψ: 1-methyl-pseudouridine; m6A: N6-methyladenosine; N4-

631 Ac-C: N4-acetylcytidine; UTR: untranslated sequences; poly(A): polyadenylate; SHAPE-MaP:
632 selective 2' hydroxyl acylation analyzed by primer extension and mutational profiling; UPA: UX1
633 plus PABP motif; RIP: RNA immunoprecipitation; BMDC: bone marrow-derived dendritic cell;
634 TLRs: Toll-like receptors; PRRs: pattern recognition receptors; GSEA: gene set enrichment analysis;
635 ALT: alanine aminotransferase; AST: aspartate aminotransferase; H&E: hematoxylin and eosin;
636 PBMCs: peripheral blood mononuclear cells; OVA: ovalbumin; HPV: human papillomavirus; RFS:
637 recurrence-free survival
638

639 **DATA AND CODE AVAILABILITY**

640 The authors declare that all data supporting the findings of this study are available within the article
641 and its supplemental files or are available from the authors upon request.
642

643 **ACKNOWLEDGMENTS**

644 This work was supported by grants from National Key Research and Development Project of China
645 (2021YFA1300500), National Natural Science Foundation of China (82272625), and Fujian
646 provincial health technology project (2024ZD01004).
647

648 **AUTHOR CONTRIBUTIONS**

649 S.H., H.Y., Z.H. and Z.F. designed the study; H.Y. performed the experiments and analyzed the data;
650 Y.Y., C.L., and Y.W. helped with some of the experiments; P.L. helped with the RNA-seq data
651 analysis; H.Y., S.H. and Z.H. wrote and revised the manuscript. All authors have read and agreed to

652 the published version of the manuscript.

653

654 **DECLARATION OF INTERESTS**

655 S.H. and H.Y. are listed as inventors of the application of LciRNA platform.

656

657 **REFERENCES**

658

659 1. Baden, L. R. *et al.* Efficacy and Safety of the mRNA-1273 SARS-CoV-2 Vaccine.
660 *N Engl J Med* **384**, 403–416 (2021).
661 2. Sayour, E. J., Boczkowski, D., Mitchell, D. A. & Nair, S. K. Cancer mRNA
662 vaccines: clinical advances and future opportunities. *Nat Rev Clin Oncol* **21**, 489–500
663 (2024).
664 3. Zhou, Y., Wei, Y., Tian, X. & Wei, X. Cancer vaccines: current status and future
665 directions. *J Hematol Oncol* **18**, 18 (2025).
666 4. Weber, J. S. *et al.* Individualised neoantigen therapy mRNA-4157 (V940) plus
667 pembrolizumab versus pembrolizumab monotherapy in resected melanoma
668 (KEYNOTE-942): a randomised, phase 2b study. *Lancet* **403**, 632–644 (2024).
669 5. Rojas, L. A. *et al.* Personalized RNA neoantigen vaccines stimulate T cells in
670 pancreatic cancer. *Nature* **618**, 144–150 (2023).
671 6. Sethna, Z. *et al.* RNA neoantigen vaccines prime long-lived CD8+ T cells in
672 pancreatic cancer. *Nature* (2025) doi:10.1038/s41586-024-08508-4.
673 7. Rohner, E., Yang, R., Foo, K. S., Goedel, A. & Chien, K. R. Unlocking the promise
674 of mRNA therapeutics. *Nat Biotechnol* **40**, 1586–1600 (2022).
675 8. Wesselhoeft, R. A., Kowalski, P. S. & Anderson, D. G. Engineering circular RNA
676 for potent and stable translation in eukaryotic cells. *Nat Commun* **9**, 2629 (2018).
677 9. Yu, H. *et al.* Optimized circular RNA vaccines for superior cancer immunotherapy.
678 *Theranostics* **15**, 1420–1438 (2025).
679 10. Obi, P. & Chen, Y. G. The design and synthesis of circular RNAs. *Methods* **196**,
680 85–103 (2021).
681 11. Niu, D., Wu, Y. & Lian, J. Circular RNA vaccine in disease prevention and

682 treatment. *Signal Transduct Target Ther* **8**, 341 (2023).
683 12. Fuller, D. H. & Berglund, P. Amplifying RNA Vaccine Development. *N. Engl. J.*
684 *Med.* **382**, 2469–2471 (2020).
685 13. Minnaert, A.-K. *et al.* Strategies for controlling the innate immune activity of
686 conventional and self-amplifying mRNA therapeutics: Getting the message across. *Adv.*
687 *Drug Delivery Rev.* **176**, 113900 (2021).
688 14. Casmil, I. C. *et al.* The advent of clinical self-amplifying RNA vaccines. *Mol. Ther.*
689 **33**, 2565–2582 (2025).
690 15. Chen, H. *et al.* Branched chemically modified poly(A) tails enhance the translation
691 capacity of mRNA. *Nat Biotechnol* **43**, 194–203 (2025).
692 16. Chen, H. *et al.* Chemical and topological design of multicapped mRNA and capped
693 circular RNA to augment translation. *Nat Biotechnol* (2024) doi:10.1038/s41587-024-
694 02393-y.
695 17. Szabó, G. T., Mahiny, A. J. & Vlatkovic, I. COVID-19 mRNA vaccines: Platforms
696 and current developments. *Mol. Ther.* **30**, 1850–1868 (2022).
697 18. Ramanathan, A., Robb, G. B. & Chan, S.-H. mRNA capping: biological functions
698 and applications. *Nucleic Acids Res.* **44**, 7511–7526 (2016).
699 19. Henderson, J. M. *et al.* Cap 1 Messenger RNA Synthesis with Co-transcriptional
700 CleanCap® Analog by In Vitro Transcription. *Curr Protoc* **1**, e39 (2021).
701 20. Karikó, K. *et al.* Incorporation of pseudouridine into mRNA yields superior
702 nonimmunogenic vector with increased translational capacity and biological stability.
703 *Mol. Ther.* **16**, 1833–1840 (2008).
704 21. Andries, O. *et al.* N(1)-methylpseudouridine-incorporated mRNA outperforms
705 pseudouridine-incorporated mRNA by providing enhanced protein expression and
706 reduced immunogenicity in mammalian cell lines and mice. *J Control Release* **217**,
707 337–344 (2015).
708 22. Huang, J. *et al.* Preclinical Efficacy of Cap-Dependent and Independent mRNA
709 Vaccines against Bovine Viral Diarrhea Virus-1. *Vet. Sci.* **11**, 373 (2024).
710 23. Zheng, X. *et al.* Development and application of an uncapped mRNA platform.
711 *Ann Med* **57**, 2437046 (2025).
712 24. Solodushko, V., Kim, J. H. & Fouty, B. A capless hairpin-protected mRNA vaccine
713 encoding the full-length Influenza A hemagglutinin protects mice against a lethal
714 Influenza A infection. *Gene Ther.* (2025) doi:10.1038/s41434-025-00521-0.
715 25. Sonneveld, S., Verhagen, B. M. P. & Tanenbaum, M. E. Heterogeneity in mRNA

716 Translation. *Trends Cell Biol.* **30**, 606–618 (2020).
717 26. Akiyama, T., Suzuki, T. & Yamamoto, T. RNA decay machinery safeguards
718 immune cell development and immunological responses. *Trends Immunol* **42**, 447–460
719 (2021).
720 27. Villordo, S. M., Carballeda, J. M., Filomatori, C. V. & Gamarnik, A. V. RNA
721 Structure Duplications and Flavivirus Host Adaptation. *Trends Microbiol* **24**, 270–283
722 (2016).
723 28. Slonchak, A. & Khromykh, A. A. Subgenomic flaviviral RNAs: What do we know
724 after the first decade of research. *Antiviral Res* **159**, 13–25 (2018).
725 29. Passmore, L. A. & Coller, J. Roles of mRNA poly(A) tails in regulation of
726 eukaryotic gene expression. *Nat Rev Mol Cell Biol* **23**, 93–106 (2022).
727 30. Zhu, T.-Y., Hong, L.-L. & Ling, Z.-Q. Oncofetal protein IGF2BPs in human cancer:
728 functions, mechanisms and therapeutic potential. *Biomarker Res.* **11**, 62 (2023).
729 31. Chapman, E. G., Moon, S. L., Wilusz, J. & Kieft, J. S. RNA structures that resist
730 degradation by Xrn1 produce a pathogenic Dengue virus RNA. *eLife* **3**, e01892 (2014).
731 32. Graham, M. E. *et al.* Zika virus dumbbell-1 structure is critical for sfRNA presence
732 and cytopathic effect during infection. *Mbio* **14**, e0110823 (2023).
733 33. Gruber, A. R., Lorenz, R., Bernhart, S. H., Neubock, R. & Hofacker, I. L. The
734 Vienna RNA Websuite. *Nucleic Acids Res.* **36**, W70–W74 (2008).
735 34. Svitkin, Y. V. *et al.* N1-methyl-pseudouridine in mRNA enhances translation
736 through eIF2α-dependent and independent mechanisms by increasing ribosome density.
737 *Nucleic Acids Res* **45**, 6023–6036 (2017).
738 35. Chen, R. *et al.* Engineering circular RNA for enhanced protein production. *Nat*
739 *Biotechnol* **41**, 262–272 (2023).
740 36. Hao, H. *et al.* N4-acetylcytidine regulates the replication and pathogenicity of
741 enterovirus 71. *Nucleic Acids Res.* **50**, 9339–9354 (2022).
742 37. Harcourt, E. M., Kietrys, A. M. & Kool, E. T. Chemical and structural effects of
743 base modifications in messenger RNA. *Nature* **541**, 339–346 (2017).
744 38. Niu, X. *et al.* Pseudoknot length modulates the folding, conformational dynamics,
745 and robustness of Xrn1 resistance of flaviviral xrRNAs. *Nat Commun* **12**, 6417 (2021).
746 39. Leppek, K. & Stoecklin, G. An optimized streptavidin-binding RNA aptamer for
747 purification of ribonucleoprotein complexes identifies novel ARE-binding proteins.
748 *Nucleic Acids Research* **42**, e13 (2014).
749 40. Reichman, T. W., Muñiz, L. C. & Mathews, M. B. The RNA Binding Protein

750 Nuclear Factor 90 Functions as Both a Positive and Negative Regulator of Gene
751 Expression in Mammalian Cells. *Mol. Cell. Biol.* **22**, 343–356 (2002).
752 41. Harashima, A., Guettouche, T. & Barber, G. N. Phosphorylation of the NFAR
753 proteins by the dsRNA-dependent protein kinase PKR constitutes a novel mechanism
754 of translational regulation and cellular defense. *Genes Dev* **24**, 2640–2653 (2010).
755 42. Castella, S., Bernard, R., Corno, M., Fradin, A. & Larcher, J.-C. Ilf3 and NF90
756 functions in RNA biology. *Wiley Interdiscip Rev RNA* **6**, 243–256 (2015).
757 43. Kang, J.-I. *et al.* PKR protein kinase is activated by hepatitis C virus and inhibits
758 viral replication through translational control. *Virus Res* **142**, 51–56 (2009).
759 44. Yin, X. *et al.* ILF2 Contributes to Hyperproliferation of Keratinocytes and Skin
760 Inflammation in a KLHDC7B-DT-Dependent Manner in Psoriasis. *Front. Genet.* **13**,
761 (2022).
762 45. Huang, X. *et al.* Insulin-like growth factor 2 mRNA-binding protein 1 (IGF2BP1)
763 in cancer. *J Hematol Oncol* **11**, 88 (2018).
764 46. Dinh, N. T. M., Nguyen, T. M., Park, M. K. & Lee, C. H. Y-Box Binding Protein
765 1: Unraveling the Multifaceted Role in Cancer Development and Therapeutic Potential.
766 *Int J Mol Sci* **25**, 717 (2024).
767 47. Okumura, F. *et al.* Activation of double-stranded RNA-activated protein kinase
768 (PKR) by interferon-stimulated gene 15 (ISG15) modification down-regulates protein
769 translation. *J Biol Chem* **288**, 2839–2847 (2013).
770 48. Guan, D. *et al.* Nuclear Factor 45 (NF45) Is a Regulatory Subunit of Complexes
771 with NF90/110 Involved in Mitotic Control. *Molecular and Cellular Biology* **28**, 4629–
772 4641 (2008).
773 49. Nourreddine, S. *et al.* NF45 and NF90 Regulate Mitotic Gene Expression by
774 Competing with Staufen-Mediated mRNA Decay. *Cell Reports* **31**, 107660 (2020).
775 50. Guasp, P., Reiche, C., Sethna, Z. & Balachandran, V. P. RNA vaccines for cancer:
776 Principles to practice. *Cancer Cell* **42**, 1163–1184 (2024).
777 51. Verbeke, R., Hogan, M. J., Loré, K. & Pardi, N. Innate immune mechanisms of
778 mRNA vaccines. *Immunity* **55**, 1993–2005 (2022).
779 52. Rehwinkel, J. & Gack, M. U. RIG-I-like receptors: their regulation and roles in
780 RNA sensing. *Nat. Rev. Immunol.* **20**, 537–551 (2020).
781 53. Liu, C.-X. *et al.* RNA circles with minimized immunogenicity as potent PKR
782 inhibitors. *Mol Cell* **82**, 420-434.e6 (2022).
783 54. Chen, Y. G. *et al.* Sensing Self and Foreign Circular RNAs by Intron Identity. *Mol*

Cell **67**, 228-238.e5 (2017).

55. Duan, T., Du, Y., Xing, C., Wang, H. Y. & Wang, R.-F. Toll-Like Receptor Signaling and Its Role in Cell-Mediated Immunity. *Front. Immunol.* **13**, 812774 (2022).

56. Nazitto, R. *et al.* ILF3 Is a Negative Transcriptional Regulator of Innate Immune Responses and Myeloid Dendritic Cell Maturation. *J. Immunol.* **206**, 2949–2965 (2021).

57. Dalod, M., Chelbi, R., Malissen, B. & Lawrence, T. Dendritic cell maturation: functional specialization through signaling specificity and transcriptional programming. *EMBO J.* **33**, 1104–1116 (2014).

58. Burd, E. M. Human papillomavirus and cervical cancer. *Clin Microbiol Rev* **16**, 1–17 (2003).

59. de Sanjosé, S., Bruni, L. & Alemany, L. HPV in genital cancers (at the exception of cervical cancer) and anal cancers. *Presse Med* **43**, e423-428 (2014).

60. Jinek, M., Coyle, S. M. & Doudna, J. A. Coupled 5' nucleotide recognition and processivity in Xrn1-mediated mRNA decay. *Mol. Cell* **41**, 600–608 (2011).

61. Chang, J. H., Xiang, S., Xiang, K., Manley, J. L. & Tong, L. Structural and biochemical studies of the 5′→3′ exoribonuclease Xrn1. *Nat. Struct. Mol. Biol.* **18**, 270–276 (2011).

62. Binnewies, M. *et al.* Understanding the tumor immune microenvironment (TIME) for effective therapy. *Nat. Med.* **24**, 541–550 (2018).

63. Li, N. *et al.* ILF2 promotes anchorage independence through direct regulation of PTEN. *Oncol. Lett.* **18**, 1689–1696 (2019).

64. Du, H., Le, Y., Sun, F., Li, K. & Xu, Y. ILF2 Directly Binds and Stabilizes CREB to Stimulate Malignant Phenotypes of Liver Cancer Cells. *Anal. Cell. Pathol.* **2019**, 1–9 (2019).

65. Smola, M. J., Rice, G. M., Busan, S., Siegfried, N. A. & Weeks, K. M. Selective 2'-hydroxyl acylation analyzed by primer extension and mutational profiling (SHAPE-MaP) for direct, versatile and accurate RNA structure analysis. *Nat Protoc* **10**, 1643–1669 (2015).

66. Mb, L. *et al.* An advanced culture method for generating large quantities of highly pure dendritic cells from mouse bone marrow. *Journal of immunological methods* **223**, (1999).

816 **Figure Legends**

817

818 **Figure 1. Engineering LciRNA with Flaviviral xrRNA and PABP Motif for Enhanced Stability**

819 **and Translation.**

820 (A) Schematic diagram of LciRNA design. XRN-1 resissting structures of sfRNA and PABP binding

821 motif are placed at the 5' end to protect LciRNA from degradation, with EV-A-S1 downstream to

822 initiate translation. (B) Schematic diagram of XRN-1 resisting structures in sfRNA of CFAV, DENV,

823 USUV, YFV and ZIKV. xrRNA structures are in red; Dumbbell structures are in green. (C)

824 Comparison of Gluc activity between Gluc LciRNAs with individual structure in (B) or without any

825 XRN-1 resisting structures (Indicated as IRES). (D) Schematic diagram of untranslated regions

826 screened. (E) Comparison of Gluc activity between Gluc LciRNAs with PABP motif, poly cytosine

827 (polyC), poly thymine (polyT) or with no nucleotides (Empty) in the region between UX1 and EV-

828 A-S1. (F) Comparison of Gluc activity between Gluc LciRNAs with indicated 3'UTR. (G)

829 Comparison of Gluc activity between Gluc LciRNAs with indicated 5'UTR or without any

830 nucleotides (Empty). All data are mean (SD) for n= 3 biological replicates. One-way ANOVA was

831 used to calculate the statistical significance. *P < 0.05 was considered statistically significant. **P

832 < 0.01, ***P < 0.001 and ****P < 0.0001 were considered highly significant. ns, not significant.

833

834 **Figure 2. Engineered LciRNA Outperforms m1Ψ-modified Capped mRNA in *in vivo***

835 **Persistence.**

836 (A) Comparison of Gluc activity between Gluc LciRNAs with indicated percentages of m6A, m1Ψ

837 and N4-Ac-C modified nucleotides. (B) Secondary structure of UX1. The nucleotide coloring
838 indicates normalized reactivity values of <=0.4(gray), >0.4 and <0.85 (light red), and >=0.85 (dark
839 red). Bold black characters indicate pseudoknots. (C) Comparison of Gluc activity between Gluc
840 LciRNAs with indicated UX1 mutants or wildtype UX1. (D) Comparison of Gluc activity between
841 Gluc LciRNAs with indicated 5' end protective sequences (UPA, 2UPA, 3UPA, P-IRES (with only
842 PABP motif) and IRES), capped Gluc mRNA (CAP) and 100% m1Ψ modified capped mRNA
843 (mCAP). (E) Relative Gluc activity of indicated RNAs from day 1 to 5. (F) *In vivo* fluorescence
844 images of mice at indicated time after injection of indicated Fluc RNA-LNP. (G) Total Flux data
845 corresponding to the images in (F). (H) Area under curve analysis of Total Flux data from 48 h to
846 120 h in (G). All data are mean (SD) for n= 3 biological replicates. One-way ANOVA was used to
847 calculate the statistical significance. *P < 0.05 was considered statistically significant. **P < 0.01,
848 ***P < 0.001 and ****P < 0.0001 were considered highly significant. ns, not significant.
849
850 **Figure 3. UPA Sequence Stabilizes LciRNA Through XRN-1 Inhibition and RBP Binding.**
851 (A) Schematic diagram of XRN-1 *in vitro* digestion assay. XRN-1 and RppH were added together
852 to digest the indicated RNAs. (B) 2% agarose gel analysis of RNAs after 2 hours of XRN-1 digestion.
853 right panel: representative gel image; left panel: quantification of three independent experiments.
854 (C) Schematic diagram of experimental procedures to identify UPA specific RBPs. Briefly,
855 uncapped RNA with UPA plus SA-aptamer sequences or SA-aptamer alone were incubated with
856 streptavidin beads to pull-down interacting proteins, after which mass spectrometry, western blot,
857 RNA immunoprecipitation analysis and functional assays were conducted to verify RBPs' binding

858 and function. (D) Silver-stained gel of proteins isolated by RNA pull-down assay. Red arrows
859 highlight UPA specific bands. (E) Western blot validation results of potential UPA sequence binding
860 proteins. (F) RNA immunoprecipitation-qPCR (RIP-qPCR) results of potential UPA-binding
861 proteins in Hela cells. Numbers above the bars indicate folds of UPA RNA levels to that of IgG
862 control group. (G) Relative RNA levels quantified by qPCR after siRNA-mediated knockdown of
863 the corresponding genes. Hela cells were treated with siRNAs targeting specific genes for 48 hours
864 prior to qPCR analysis. (H), (I), (J) Relative Gluc activity of three types of GLUC RNAs in Hela
865 cells with siRNA knockdown of the corresponding genes, compared to non-knockdown cells. Hela
866 cells were treated with siRNAs targeting specific genes for 48 hours, followed by transfection with
867 UPA LciRNA, LciRNA containing only IRES, or 100% m1Ψ modified capped mRNA (mCAP).
868 GLUC activity was assessed 24 hours post-transfection. All data are mean (SD) for n = 3 biological
869 replicates. For (B) One-way ANOVA was used to calculate the statistical significance. For (G)-(J)
870 two-tailed unpaired Student's t-test was used to calculate the statistical significance. *P < 0.05 was
871 considered statistically significant. **P < 0.01, ***P < 0.001 and ****P < 0.0001 were considered
872 highly significant. ns, not significant.
873
874 **Figure 4. Self-Adjuvanting LciRNA Drives PRR-Mediated DC Maturation with Minimal**
875 **Toxicity.**
876 (A) Normalized RNA levels of BMDCs transfected with indicated LciRNAs (UPA-Fluc, 2UPA-
877 Fluc), capped mRNAs (CAP-Fluc, 100% m1Ψ modified mCAP-Fluc) or empty transfection reagent
878 (Control) for 24 hours. Data were measured by RT-qPCR. The statistical significance was assessed

879 between Control and indicated groups. (B) Heatmap of normalized mRNA expression levels of
880 differentially expressed genes involved in antigen processing & presentation, RIG-1 signaling, TLR
881 signaling, T cell activation, response to type-I interferon, inflammatory response to antigenic
882 stimulus and cytokine production involved in inflammation. Columns represent individual genes
883 and rows represent experimental samples (n = 3 biological replicates per group). TPM values were
884 scaled by column to standardize gene-wise expression patterns, with color intensity indicating
885 relative expression levels (blue, low expression; red, high expression). (C) GSEA plots showing the
886 most-enriched immune response related KEGG pathways in the 2UPA group. FDR stands for false
887 discovery rate. NES stands for normalized enrichment score. (D) Body weight of mice after
888 intramuscular injection of UPA-E6E7, 2UPA-E6E7, or mCAP-E6E7 vaccines. (2 doses 5 μg per
889 dose, black arrow indicated injection time). (E) & (F) Serum ALT (E), AST(F) levels in mice before
890 and after administration of two vaccine doses. ("Before Vac." indicates before vaccination, while
891 "1st dose" and "2nd dose" means 7 days after the first and second doses, respectively.) (G)
892 Histological staining of major organs two weeks after the second vaccine dose (scale bar = 1mm).
893 All data are mean (SD) for n = 3 biological replicates. One-way ANOVA was used to calculate the
894 statistical significance. *P < 0.05 was considered statistically significant. **P < 0.01, ***P < 0.001
895 and ****P < 0.0001 were considered highly significant. ns, not significant.
896
897 **Figure 5. LciRNA Vaccination Provokes Potent Tumor-Specific T Cell Responses and Inhibits**
898 **B16F10-OVA Melanoma Growth.**
899 (A) Timeline of tumor inoculation, vaccination, and blood and tissue sample collection. Mice were

900 subcutaneously inoculated with 1×10^5 B16F10-OVA cells and intramuscularly injected with mCAP-
901 Fluc, UPA-OVA, 2UPA-OVA, or mCAP-OVA vaccines (3 μg per mouse, n = 6 for each group) on
902 day 3 and day 10. (B) Tumor volumes from day 0 to day 20 after tumor inoculation. Statistical
903 significance was calculated based on tumor volumes data on day 20. (C) Photographs of tumors
904 excised after euthanasia on day 20 post-tumor inoculation, with red circles indicating complete
905 tumor regression in mice. (D) Proportion of OVA-specific CD8+ T cells in PBMCs one week after
906 the second vaccine dose (OVA peptide MHC tetramer-positive). (E) Representative flow cytometry
907 plots for (D). (F) Proportion of OVA-specific CD8+ T cells in the spleen 10 days after the second
908 vaccine dose (IFN-γ-positive T cells after transfection with OVA mRNA). (G) Number of OVA-
909 specific CD8+ T cells per million cells in tumors 10 days after the second vaccine dose (OVA peptide
910 MHC tetramer-positive). (H) Number of CD4+ T cells per million cells in tumor tissue. (I) Number
911 of CD8+ T cells per million cells in tumor tissue. For (B), data are mean (SEM). All other data are
912 mean (SD) for at least 3 biological replicates. One-way ANOVA was used to calculate the statistical
913 significance. *$P < 0.05$ was considered statistically significant. **$P < 0.01$, ***$P < 0.001$ and ****P
914 < 0.0001 were considered highly significant. ns, not significant.
915
916 **Figure 6. Effective Clearance of HPV associated Tumors by LciRNA-Based Therapeutic**
917 **Vaccination.**
918 (A) Timeline of tumor inoculation, vaccination, and blood and tissue sample collection. Mice were
919 subcutaneously inoculated with 5×10^5 TC-1 cells, and when the average tumor volume reached
920 approximately 50 mm^3 on day 9, they were intramuscularly injected with mCAP-Fluc, UPA-E6E7,

921 2UPA-E6E7, or mCAP-E6E7 vaccines (3 μg per mouse, n = 6 for each group), followed by a second
922 dose (3 μg per mouse) one week later (day 16). (B)Tumor volumes from day 0 to day 23 after tumor
923 inoculation. Statistical significance was calculated based on tumor volumes data on day 23. (C)
924 Survival rate of mice from day 0 to day 40 after tumor inoculation. (D) Proportion of E6E7-specific
925 CD8+ T cells in PBMCs one week after the second vaccine dose (IFN-γ-positive T cells after
926 stimulation with E6E7 antigen peptides). (E) Representative flow cytometry plots for (D). (F)
927 Proportion of E6E7-specific CD8+ T cells in the spleen on day 40 (IFN-γ-positive T cells after
928 transfection with E6E7 mRNA). For (B), data are mean (SEM). All other data are mean (SD) for 6
929 biological replicates. For (C) Kaplan-Meier simple survival analysis was used to calculate the
930 survival rate, and Log-rank (Mantel-Cox) test was used to calculate the statistical significance. For
931 other plots, one-way ANOVA was used to calculate the statistical significance. *P < 0.05 was
932 considered statistically significant. **P < 0.01, ***P < 0.001 and ****P < 0.0001 were considered
933 highly significant. ns, not significant.
934
935 **Figure 7. Immunostimulatory LciRNA induces optimal T cell priming.**
936 Schematic overview of T cell priming by dendritic cell (DC) after LciRNA cancer vaccine uptake.
937 Upon absorption, LciRNA is recognized by PRRs, such as RIG-I, TLRs and PKR, which activate
938 the expression of Type-I interferon and other inflammatory cytokines and chemokines, such as IL6,
939 IL12, IL15, CXCL10. Then inflammatory signaling induces maturation of DC cells with increased
940 antigen presentation and co-stimulatory protein CD40, CD80, CD86 expression. Meanwhile,
941 relative higher in cell stability of LciRNA insured longer expression of antigenic peptides. As a

942 result, all three signals of T cell activation (antigen presentation, co-stimulatory protein and
943 cytokines) coincide during T cell priming by LciRNA absorbed DC cells. Thus, immunostimulatory
944 LciRNA ensures optimal T cell priming.
945
946 **Figure S1. RNAfold predicted xrRNA and dumbbell structures of CFAV, DENV, USUV, YFV**
947 **and ZIKV.**
948 Minimum free energy (MFE) structures were predicted with RNA energy parameters of Andronescu
949 model chosen. The structures were visualized by Forna.
950
951 **Figure S2. UX1 SHAPE-MaP reactivity profile and top ranked proteins in mass**
952 **spectrometry result.**
953 (A) Bar plot of SHAPE-MaP reactivity profile of UX1. Reactivities below 0.4 are colored black,
954 reactivities between 0.4 and 0.85 are shown in orange and reactivities above 0.85 are shown in red.
955 (B) Top ranked proteins in mass spectrometry result. The red box indicates proteins distributed in
956 the cytoplasm.
957
958 **Figure S3. Heatmaps of normalized mRNA expression levels of genes upregulated in PRR**
959 **induced DC maturation, and genes of T cell co-stimulatory protein, inflammatory cytokines**
960 **and chemokines.** (A) Heatmap of normalized mRNA expression levels of genes upregulated in
961 PRR induced DC maturation. (B) Heatmap of normalized mRNA expression levels of genes of T
962 cell co-stimulatory protein, inflammatory cytokines and chemokines. Rows represent individual

963 genes and columns represent experimental samples (n=3 biological replicates per group). TPM
964 values were scaled by row to standardize gene-wise expression patterns, with color intensity
965 indicating relative expression levels (blue, low expression; red, high expression).
966
967 **Figure S4. Body weight means, tumor volumes of individual mouse and representative flow**
968 **cytometry plots of the B16F10-OVA treatment model in Figure 5.**
969 (A) Mean body weight of each group from day 0 to day 20. Data are mean (SD) of n=6 biological
970 replicates per group. (B) Tumor volumes of individual mouse from day 0 to day 20. (C)
971 Representative flow cytometry plots of Figure 5F.
972
973 **Figure S5. Gating information of Figure 5.**
974 (A), (B) and (C) are gating information of PBMCs (Figure 5D), spleens (Figure 5F), tumors (Figure
975 5G, 5H and 5I).
976
977 **Figure S6. Body weight means, tumor volumes of individual mouse and representative flow**
978 **cytometry plots of the B16F10-OVA treatment model in Figure 5.**
979 (A) Mean body weight of each group from day 0 to day 23. Data are mean (SD) of n=6 biological
980 replicates per group. (B) Photographs of mice tumors on day 23. (C) Tumor volumes of individual
981 mouse from day 0 to day 23.
982
983 **Figure S7. Representative flow cytometry plots and gating information of Figure 6.**

984 (A) Representative flow cytometry plots of Figure 6F. (B) Gating information of PBMCs in Figure

985 6D. (C) Gating information of PBMCs in Figure 6F.

986

987 **Table S1. xrRNA, Dumbbell, IRES, UPA and UTR sequences**

988 **Table S2. Aptamer, Reporter and Vaccine sequences**

989 **Table S3. siRNA**

990 **Table S4. qPCR primers**

991

Figure 1

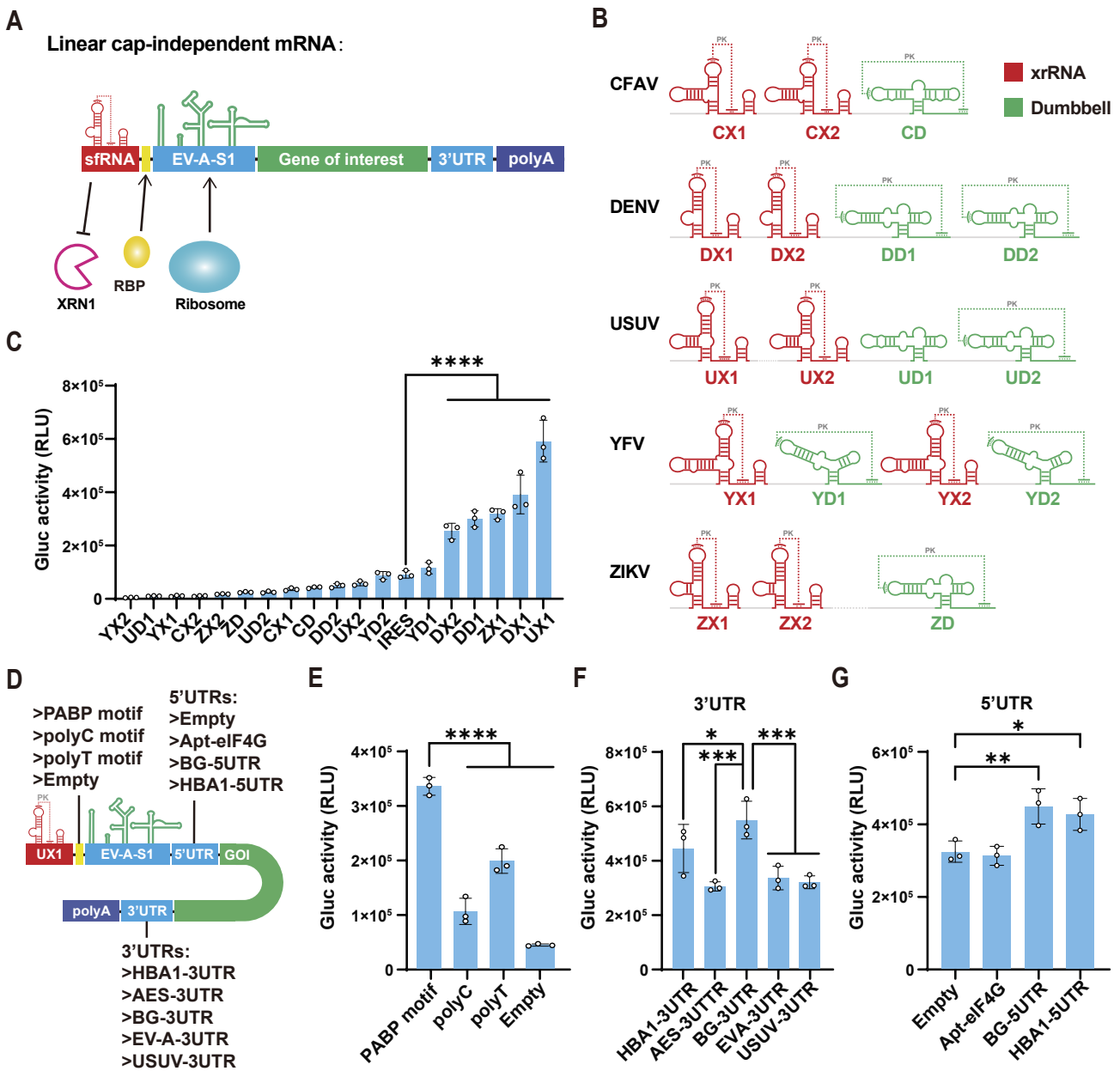
A
Linear cap-independent mRNA:
sfRNA
EV-A-S1
Gene of interest
3'UTR
polyA
XRN1
RBP
Ribosome
B
CFAV
CX1
CX2
CD
DENV
DX1
DX2
DD1
DD2
USUV
UX1
UX2
UD1
UD2
YFV
YX1
YD1
YX2
YD2
ZIKV
ZX1
ZX2
ZD
xrRNA
Dumbbell
C
Gluc activity (RLU)
8×10⁵
6×10⁵
4×10⁵
2×10⁵
0
****
YX2
UD1
YX1
CX2
ZX2
ZD
UD2
CX1
CD
DD2
UX2
YD2
IRES
YD1
DX2
DD1
ZX1
DX1
UX1
D
>PABP motif
>polyC motif
>polyT motif
>Empty
5'UTRs:
>Empty
>Apt-eIF4G
>BG-5UTR
>HBA1-5UTR
UX1
EV-A-S1
5'UTR
GOI
polyA
3'UTR
3'UTRs:
>HBA1-3UTR
>AES-3UTR
>BG-3UTR
>EV-A-3UTR
>USUV-3UTR
E
Gluc activity (RLU)
4×10⁵
3×10⁵
2×10⁵
1×10⁵
0
****
PABP motif
polyC
polyT
Empty
F
3'UTR
Gluc activity (RLU)
8×10⁵
6×10⁵
4×10⁵
2×10⁵
0
*
***
***
HBA1-3UTR
AES-3UTTR
BG-3UTR
EVA-3UTR
USUV-3UTR
G
5'UTR
Gluc activity (RLU)
6×10⁵
4×10⁵
2×10⁵
0
*
**
Empty
Apt-eIF4G
BG-5UTR
HBA1-5UTR

Figure 2

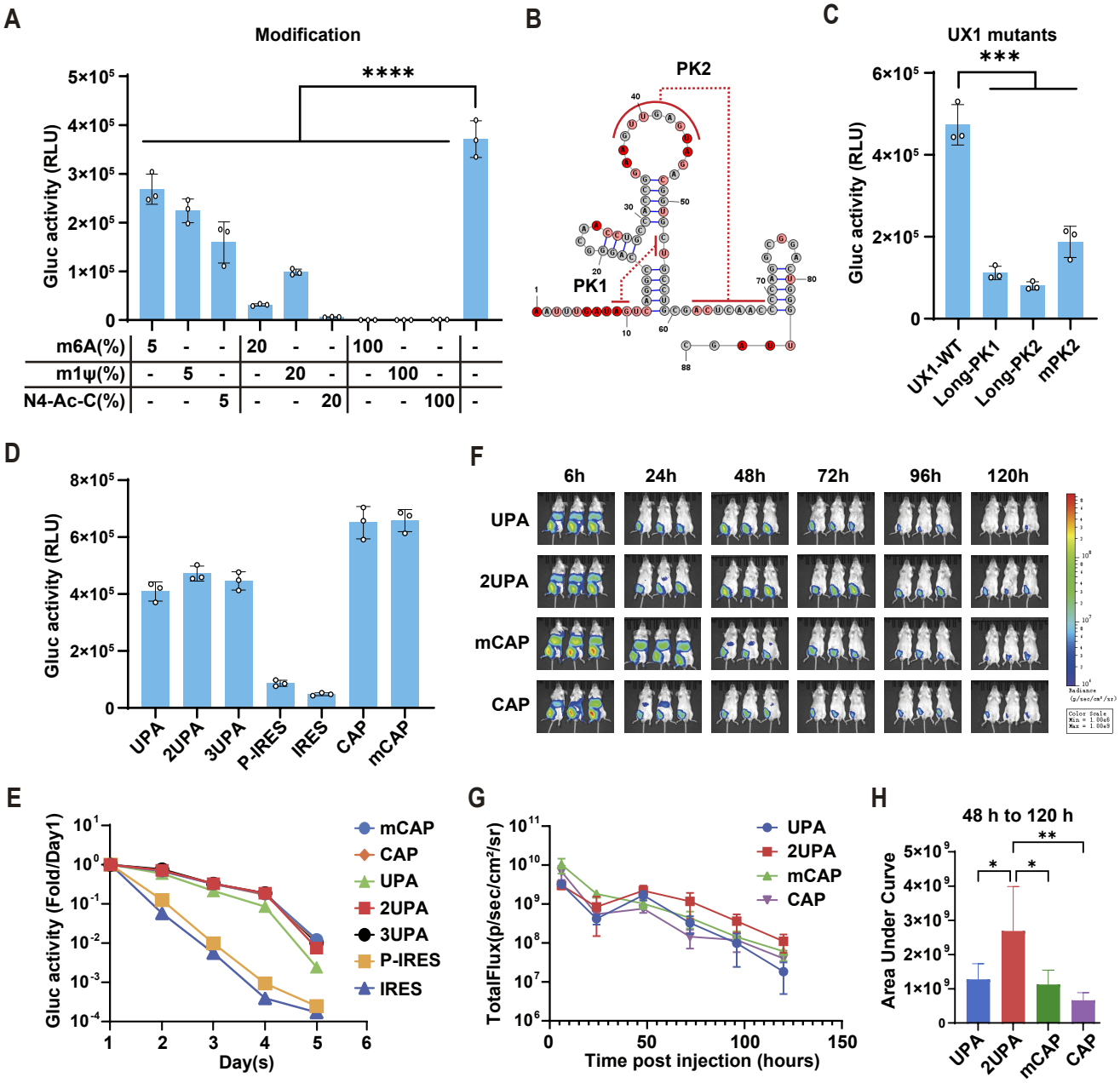
A
Modification
****
Gluc activity (RLU)
5×10^5
4×10^5
3×10^5
2×10^5
1×10^5
0
m6A(%) 5 - - 20 - - 100 - - -
m1ψ(%) - 5 - - 20 - - 100 - -
N4-Ac-C(%) - - 5 - - 20 - - 100 -
B
PK2
PK1
C
UX1 mutants
***
Gluc activity (RLU)
6×10^5
4×10^5
2×10^5
0
UX1-WT
Long-PK1
Long-PK2
mPK2
D
Gluc activity (RLU)
8×10^5
6×10^5
4×10^5
2×10^5
0
UPA
2UPA
3UPA
P-IRES
IRES
CAP
mCAP
F
6h
24h
48h
72h
96h
120h
UPA
2UPA
mCAP
CAP
E
Gluc activity (Fold/Day1)
Day(s)
mCAP
CAP
UPA
2UPA
3UPA
P-IRES
IRES
G
TotalFlux(p/sec/cm²/sr)
Time post injection (hours)
UPA
2UPA
mCAP
CAP
H
48 h to 120 h
Area Under Curve
UPA
2UPA
mCAP
CAP

Figure 3

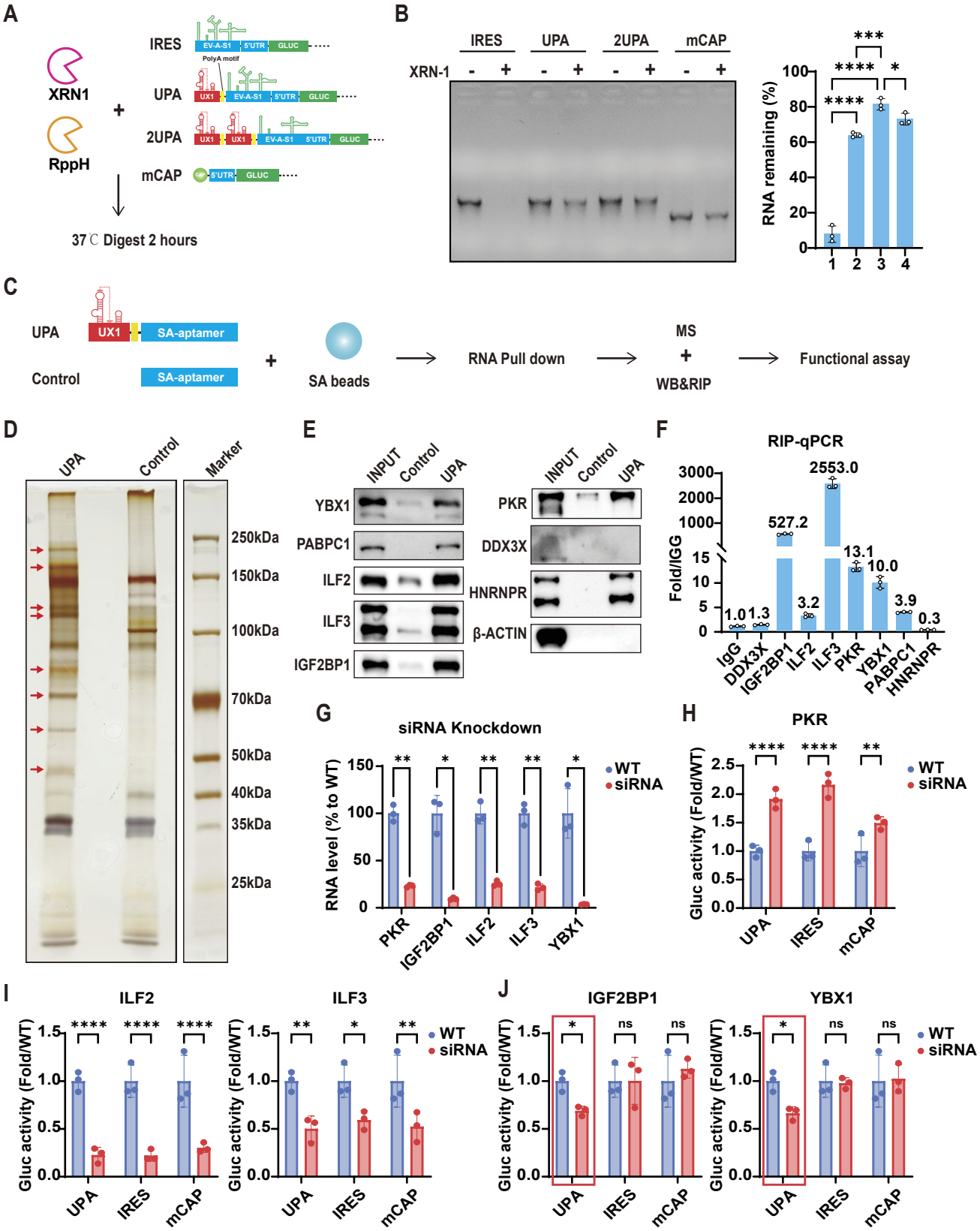
A
XRN1
RppH
IRES
UPA
2UPA
mCAP
EV-A-S1
5'UTR
GLUC
PolyA motif
UX1
37℃ Digest 2 hours
B
IRES
UPA
2UPA
mCAP
XRN-1
RNA remaining (%)
C
UPA
UX1
SA-aptamer
Control
SA beads
RNA Pull down
MS
WB&RIP
Functional assay
D
UPA
Control
Marker
250kDa
150kDa
100kDa
70kDa
50kDa
40kDa
35kDa
25kDa
E
INPUT
Control
UPA
YBX1
PABPC1
ILF2
ILF3
IGF2BP1
PKR
DDX3X
HNRNPR
β-ACTIN
F
RIP-qPCR
Fold/IGG
IgG
DDX3X
IGF2BP1
ILF2
ILF3
PKR
YBX1
PABPC1
HNRNPR
1.0
1.3
527.2
3.2
2553.0
13.1
10.0
3.9
0.3
G
siRNA Knockdown
RNA level (% to WT)
WT
siRNA
PKR
IGF2BP1
ILF2
ILF3
YBX1
H
PKR
Gluc activity (Fold/WT)
UPA
IRES
mCAP
I
ILF2
ILF3
J
IGF2BP1
YBX1
ns

Figure 4

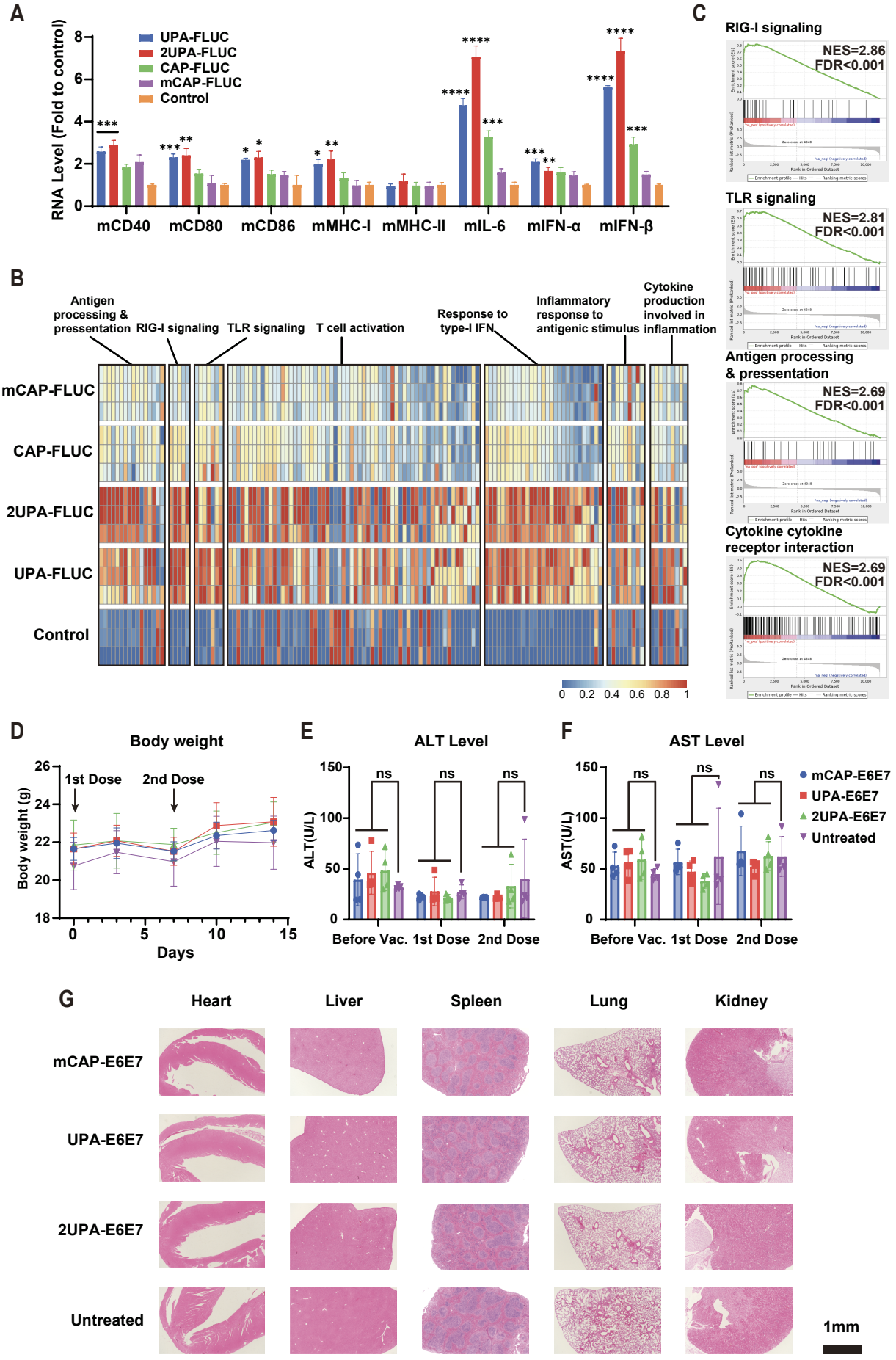
A
RNA Level (Fold to control)
UPA-FLUC
2UPA-FLUC
CAP-FLUC
mCAP-FLUC
Control
mCD40
mCD80
mCD86
mMHC-I
mMHC-II
mIL-6
mIFN-α
mIFN-β
B
Antigen processing & pressentation
RIG-I signaling
TLR signaling
T cell activation
Response to type-I IFN
Inflammatory response to antigenic stimulus
Cytokine production involved in inflammation
mCAP-FLUC
CAP-FLUC
2UPA-FLUC
UPA-FLUC
Control
C
RIG-I signaling
NES=2.86
FDR<0.001
TLR signaling
NES=2.81
FDR<0.001
Antigen processing & pressentation
NES=2.69
FDR<0.001
Cytokine cytokine receptor interaction
NES=2.69
FDR<0.001
D
Body weight
1st Dose
2nd Dose
Body weight (g)
Days
E
ALT Level
ALT(U/L)
ns
Before Vac.
1st Dose
2nd Dose
F
AST Level
AST(U/L)
mCAP-E6E7
UPA-E6E7
2UPA-E6E7
Untreated
G
Heart
Liver
Spleen
Lung
Kidney
mCAP-E6E7
UPA-E6E7
2UPA-E6E7
Untreated
1mm

Figure 5

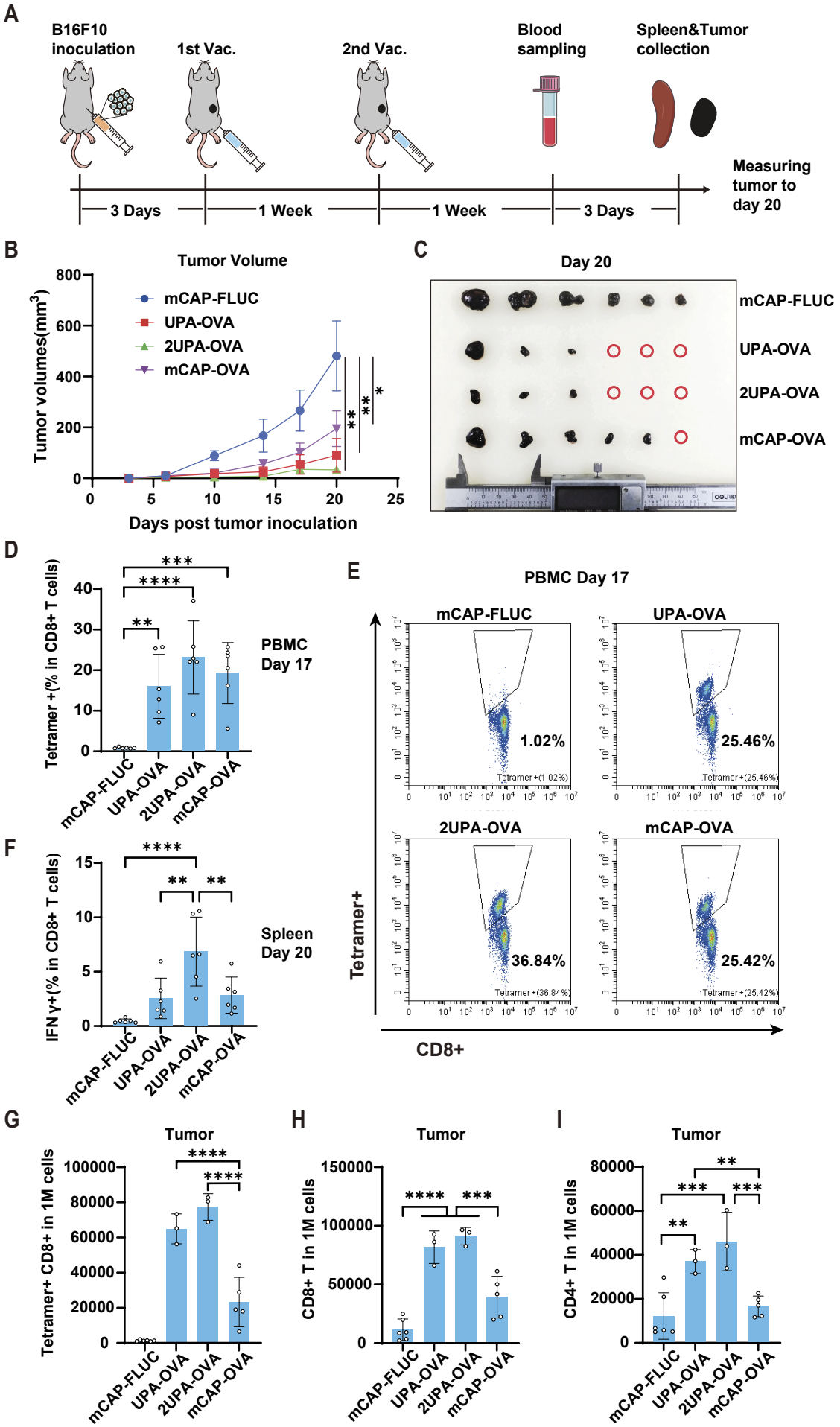
A
B16F10 inoculation
1st Vac.
2nd Vac.
Blood sampling
Spleen&Tumor collection
3 Days
1 Week
1 Week
3 Days
Measuring tumor to day 20
B
Tumor Volume
Tumor volumes(mm3)
mCAP-FLUC
UPA-OVA
2UPA-OVA
mCAP-OVA
Days post tumor inoculation
C
Day 20
mCAP-FLUC
UPA-OVA
2UPA-OVA
mCAP-OVA
D
Tetramer +(% in CD8+ T cells)
PBMC Day 17
mCAP-FLUC
UPA-OVA
2UPA-OVA
mCAP-OVA
E
PBMC Day 17
mCAP-FLUC
UPA-OVA
2UPA-OVA
mCAP-OVA
1.02%
25.46%
36.84%
25.42%
Tetramer+
CD8+
F
IFN γ+(% in CD8+ T cells)
Spleen Day 20
mCAP-FLUC
UPA-OVA
2UPA-OVA
mCAP-OVA
G
Tumor
Tetramer+ CD8+ in 1M cells
mCAP-FLUC
UPA-OVA
2UPA-OVA
mCAP-OVA
H
Tumor
CD8+ T in 1M cells
mCAP-FLUC
UPA-OVA
2UPA-OVA
mCAP-OVA
I
Tumor
CD4+ T in 1M cells
mCAP-FLUC
UPA-OVA
2UPA-OVA
mCAP-OVA

Figure 6

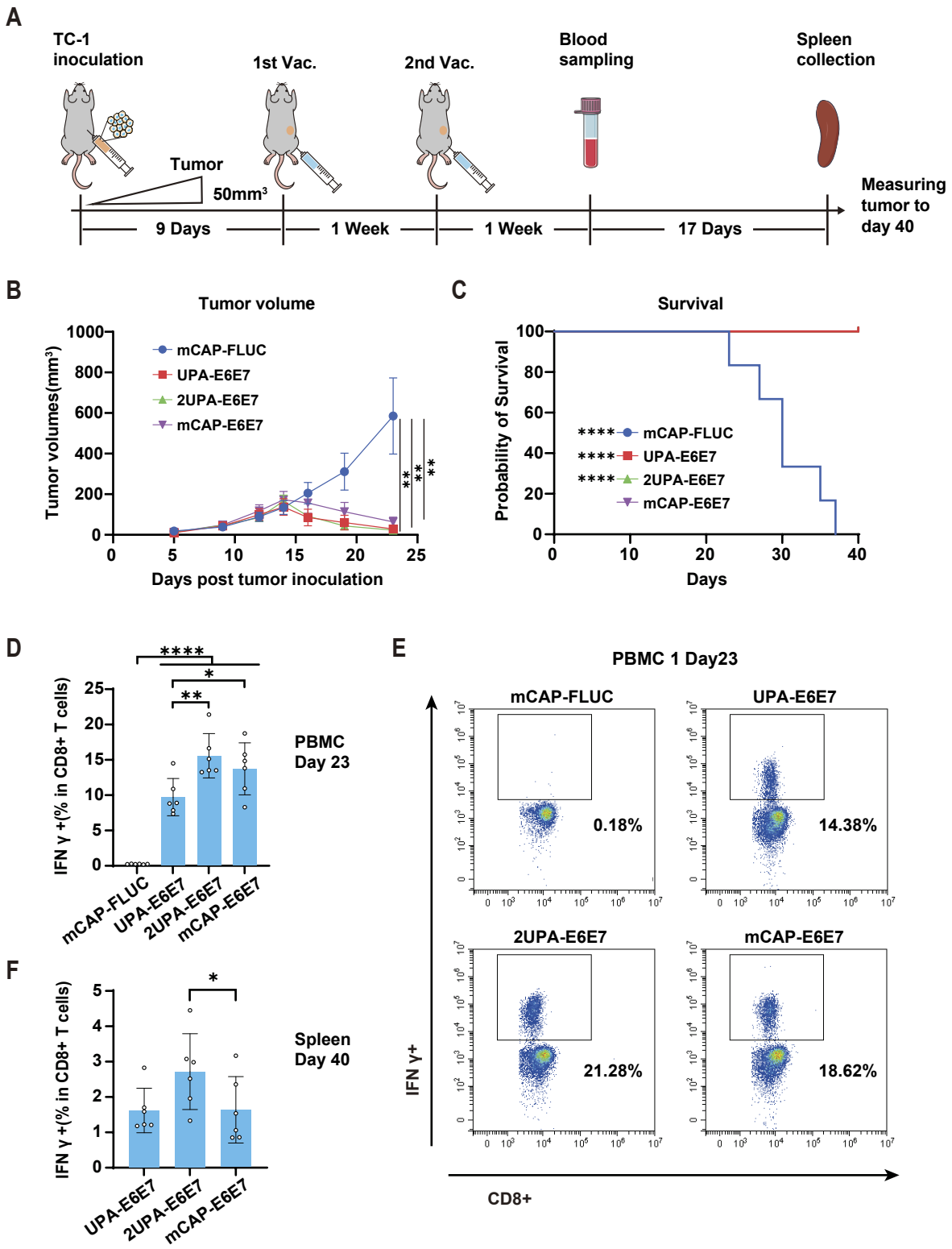
A
TC-1 inoculation
1st Vac.
2nd Vac.
Blood sampling
Spleen collection
Tumor
50mm³
Measuring tumor to day 40
9 Days
1 Week
1 Week
17 Days
B
Tumor volume
Tumor volumes(mm³)
mCAP-FLUC
UPA-E6E7
2UPA-E6E7
mCAP-E6E7
Days post tumor inoculation
C
Survival
Probability of Survival
****
Days
D
IFN γ +(% in CD8+ T cells)
PBMC Day 23
mCAP-FLUC
UPA-E6E7
2UPA-E6E7
mCAP-E6E7
E
PBMC 1 Day23
0.18%
14.38%
21.28%
18.62%
IFN γ+
CD8+
F
Spleen Day 40

Figure 7

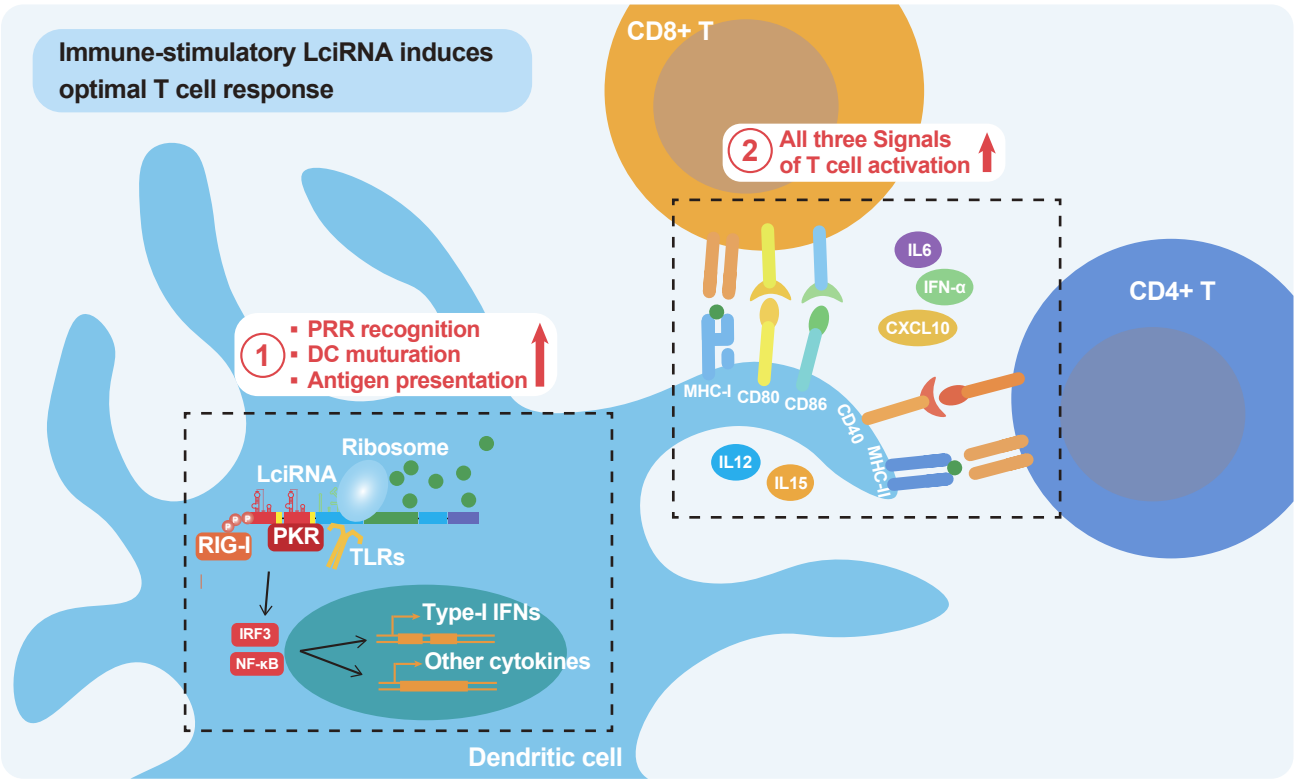
Immune-stimulatory LciRNA induces optimal T cell response
CD8+ T
2 All three Signals of T cell activation
IL6
IFN-α
CXCL10
CD4+ T
1 ▪ PRR recognition ▪ DC muturation ▪ Antigen presentation
MHC-I
CD80
CD86
CD40
MHC-II
IL12
IL15
Ribosome
LciRNA
RIG-I
PKR
TLRs
IRF3
NF-κB
Type-I IFNs
Other cytokines
Dendritic cell